

Ni- and Co-struvites: Revealing crystallization mechanism and Crystal engineering for phosphorous and transition metal recovery

Stephanos Karafiludis¹, Ana Guilherme Buzanich¹, Zdravko Kochovski², Ines Feldmann¹, Franziska Emmerling^{1,3} Tomasz M. Stawski¹

Keywords: struvite; nickel; cobalt; phosphate; phosphorous recovery; crystallization

¹Federal Institute for Materials Research and Testing, Richard-Willstätter-Straße 11, 12489 Berlin, Germany

²Soft Matter and Functional Materials, Helmholtz-Zentrum Berlin for Materials and Energy, 14109 Berlin, Germany

³Department of Chemistry, Humboldt-Universität zu Berlin, Brook-Taylor-Straße 2, 12489 Berlin

Stephanos Karafiludis: <https://orcid.org/0000-0002-7257-6311>;

Ana Guilherme Buzanich: <https://orcid.org/0000-0001-5543-9924>;

Zdravko Kochovski: <https://orcid.org/0000-0001-8375-0365> ;

Ines Feldmann: <https://orcid.org/0000-0003-2650-9270> ;

Franziska Emmerling: <https://orcid.org/0000-0001-8528-0301>;

Tomasz M. Stawski: <https://orcid.org/0000-0002-0881-5808>;

Abstract:

Waste water containing high concentrations of NH_4^+ , PO_4^{3-} and transition metals M^{2+} are environmentally harmful due to environmental pollution and toxicity. Different pathways were perused to extract hazardous transition metals or phosphate separately. Investigations on the simultaneous remove of multiple components have barely reported. We report on the use of transition metal struvite ($\text{NH}_4\text{MPO}_4 \cdot 6\text{H}_2\text{O}$, $\text{M} = \text{Ni}^{2+}$, Co^{2+}) allowing multicomponent co-precipitation. Evaluating different reaction parameters (e.g. concentration of educt solutions, pH-value, metal/phosphorous ratio) the stability of transition metal struvites, their morphologies, and sizes could be optimized. Ni-struvite is stable in a wide concentration range and at different metal/phosphorus (M/P) ratios whereas Co-struvite only forms at low M/P ratios. Detailed investigations of the precipitation process using ex situ und in situ techniques provided insights in the crystallization mechanism. Ni and Co struvite crystallizes via an intermediate colloidal nanophase which subsequently aggregates and condenses to a final crystal after longer reaction times. This mechanism is different form the immediate crystallization of μm -sized crystals ordinary struvite ($\text{NH}_4\text{MgPO}_4 \cdot 6\text{H}_2\text{O}$). The level of control of morphology and size achieved, makes transition metal struvites promising candidates for wastewater treatment and further, as precursor materials for electrochemical applications.

Introduction:

The recovery and recycling of critical and essential elements has crucial meaning for maintaining of sustainable use of raw materials. Phosphorus is an important, yet, limited natural resource. It is widely used in modern agriculture, mainly in fertilizers, but this element is not fully recyclable. In the mid-term future it could be potentially depleted as a raw material due to the high demand and rapidly declining natural phosphorite ore deposits [1, 2]. Thus, phosphate rocks are included in the European Unions' list of critical raw materials (CRMs) [3]. At the same time, due to the incomplete P-cycle in nature [4], phosphorous also causes major problems to the environment such as eutrophication of aquatic systems and is effectively lost for use. Therefore, due to simultaneous scarcity and abundance, the phosphorus recovery

from agricultural, industrial, mining, or urban waste waters have been an important factor in sustaining our global consumption and preservation of the natural environment.

In general terms phosphorous recovery relies on precipitation of P-bearing mineral phases [5, 6]. Therefore, phosphorous recovery cannot be conducted without considering the presence and the “co-recovery” of metal counter-ions. Alkaline earth metals are ubiquitous, and as such are neither of any particular interest, nor do constitute an environmental risk. In contrast, many d-block-elements are likely pollutants and/or valuable resources. These factors are especially important in the case of the controlled precipitation/crystallization of struvite from wastewater which is already a promising P-recovery route. Struvite is $\text{NH}_4\text{MPO}_4 \cdot 6\text{H}_2\text{O}$, where M^{2+} is Mg^{2+} , but other cations such as Ni^{2+} , Co^{2+} , Zn^{2+} , Cu^{2+} can substitute Mg^{2+} in the struvite structure due to similar ionic radii [7-10]. These recovered M-struvites, with $\text{M} = \text{Ni}$ and/or Co , could act as storage materials for transition metals that may be potentially up-cycled for industrial applications as raw materials for transition metal phosphate (electro)catalysts [11-14].

While the synthesis of Mg-struvite is sufficiently understood [15, 16] and used in practice [17], investigations of crystallization of transition metal struvites are scarce. Most of these studies focus on the incorporation of transition metals [18-21] or other components [22] majorly through adsorption rather than the complete substitution of magnesium in the struvite structure [18, 23-25]. Although, transition metal struvites share their fundamental crystal structure with Mg-struvite, their crystallization pathways, growth kinetics, thermodynamic stability or transformations differ among each other and from for the parent compound Mg-struvite [26, 27]. Moreover, the co-precipitation of M-struvite from solutions containing several transition metals would inevitably lead to a change in the crystallization pathway.

In transition metal phosphate recovery routes aimed at potential up-cycling, the holistic approach towards the crystallization routes is crucial. The goal is to obtain a given phase, but it should also exhibit engineered or at least predictable properties. Crystal engineering of a desired chemical compound determines its performance and scalability in industrial applications. As most transition metal phosphates precipitate fast within seconds from aqueous solutions, the crystal properties depend strongly on the precipitation parameters such as the degree of supersaturation of the educts, pH, and multiple metal cations M^{2+} in solution.

Here, we present the effect of physicochemical conditions of aqueous solutions onto the precipitation of Ni- and Co-struvites. The chosen conditions closely match those typical for several wastewater compositions. Our findings are compared with the parent Mg-struvite.

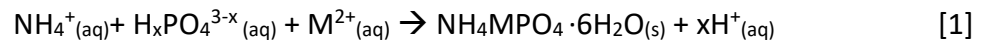
We highlight the systematic differences in crystallization pathways of Ni- and Co-struvite at all stages. The stability and speciation of the precursor phases is linked with the overall evolution of struvite crystals.

The optimized reaction conditions obtained provide an efficient M-struvite precipitation, and therefore to a significantly improved Phosphorous and transition metal recovery out of wastewaters. Based on these results tailor-made precursor materials for specific applications e.g. catalysis could be realized.

Methods

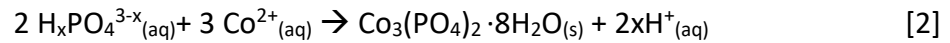
Synthesis

(NH₄)₂HPO₄ (DAP) (ChemSolute, 99%), MgCl₂·6H₂O, NiSO₄·6H₂O (ChemSolute, 99%) and CoSO₄·7H₂O (Alfa Aesar, 98 %) were used to synthesize metal phosphates under different reaction conditions from 0.004-0.3 M for NiSO₄, CoSO₄ and MgCl₂ and 0.02-0.1 mM for DAP. All detailed reaction conditions are listed in the SI (see Table S1). Our work was primarily focused on Ni and Co, but for the sake of comparison we are also synthesized and investigated common struvite (NH₄MgPO₄·6H₂O) at several selected concentrations. Based on the above-mentioned concentrations we used the metal-to-phosphate ratios (M/P) ranging for Ni and Mg from 0.02 to 3, and for Co from 0.01 to 3 to characterize each sample. At first 1 M stock solutions of DAP and the metal salts were prepared. The aqueous solutions were prepared by dissolving the calculated amount of salt in double ionized water (> 18 MΩ·cm). In a simple “one pot” approach, typically 100 ml of DAP and 100 ml of the distinct metal-bearing solution were mixed on a magnetic stirrer (300 rpm) at room temperature (25°C). The precipitation reaction of M-struvite was occurring according to the following mass-balance equation (see eq. [1]):



Eq. [1] was in general valid for Ni regardless of the metal concentration used, as well as for Co at lower concentrations below a M/P ratio of 0.4.

However, at high concentrations of Co²⁺ above a M/P ratio of 0.4 we observed the crystallization of cobalt(II)phosphate octahydrate (CPO) instead of Co-struvite (COS) according to eq. [2]):



To evaluate how the pH influences the crystal morphology, size and stability of M-struvites, sample series of Ni, Co and Mg were synthesized at different initial pH values by adding varying amounts (1-10 ml) of 1 M NaOH_(aq) or 0.1 M H₂SO_{4(aq)}. Here, we used $c(\text{M}^{2+}) = 0.02 \text{ M}$ and $c(\text{DAP}) = 0.1 \text{ M}$ to be in all systems (Ni, Co and Mg) within the phase stability field of M-struvite. For further analysis, the solid phases precipitated from the mixed solutions were collected onto a cellulose filter (pore size 1 μm, LABSOLUTE) by using a vacuum filtration kit (i.e. Büchner funnel). Afterwards the powders were left to dry in air at room temperature for two hours.

Thermodynamic calculations

All the reaction conditions were prior the experiment evaluated and verified by calculations with the aqueous geochemical simulation program PHREEQC [28] using the Lawrence Livermore National Library (llnl). Missing entries about transition metal struvites in the database were completed with data from Madsen *et. al.* 2017 [29].

pH measurements

The reaction progress was followed in situ by measuring pH as protons were released during precipitation (see eq.[1] and [2]). The pH was continuously measured with a pH electrode connected to a data logger board “DrDAQ” time resolution of 1 s processed by the Software Pico Technology (Cambridgeshire, UK).

X-ray diffraction

Powder X-ray diffraction (PXRD, XRD) data from the precipitated powders were collected on a D8 Bruker Diffractometer equipped with a LYNXEYE XE-T detector. Diffraction was measured with Cu K α radiation (1.5406 Å, 40 kV and 40 mA) from 5-60° using a step size 0.015° (2 Θ) and a scanning time of 0.5 s per step.

SEM

The scanning electron microscopy (SEM) characterization was conducted on an FEI XL 30 tungsten cathode scanning electron microscope operated at 20 keV and using a secondary electron detector. Prior to the analysis all samples were coated with a 30 nm thick layer of gold.

Dry-TEM

Dry transmission electron microscopy (TEM) images were obtained on a Talos F200S Microscope (Thermo Fisher Scientific) operating at 200kV. A Ceta 16M camera (TEM mode) and a HAADF (high angle annular dark field) detector (STEM mode; Scanning Transmission electron microscopy) were used to capture the images. Additionally, to collect detailed elemental information, energy dispersive X-ray spectroscopy was performed by two side-entry retractable silicon drift detectors (SDD). A counting time of 60 s was applied for point measurements while for elemental mappings 40-50 frames were taken resulting in a counting time of one hour. The specimen was prepared by mixing the 100 μ l educt solutions in an Eppendorf tube (1.5 ml) for 5 seconds of reaction time and dropping 10 μ l of the sample solution onto a 3 mm holey carbon-coated Cu-grid (Lacey Carbon, 400 mesh). Then the specimens were let dry at room temperature for several minutes.

Cryo-TEM

Due to beam damage these phases develop mesopores similar to what is observed in crystalline struvite after thermal heating [27]. Cryo-TEM allowed us to minimize and prevent beam damage artefacts on the material. Cryo-EM imaging was performed with a JEOL JEM-2100 transmission electron microscope (JEOL GmbH, Echting, Germany). Cryo-EM specimens were prepared by applying a 4 μ l droplet of sample solution to lacey carbon-coated copper TEM grids (200 mesh, Electron Microscopy Sciences, Hatfield, PA) and plunge-freezing them into liquid ethane using an FEI vitrobot Mark IV set at 4°C and 95% humidity. Vitrified grids were either transferred directly to the microscope cryo transfer holder (Gatan 914, Gatan, Munich, Germany) or stored in liquid nitrogen. All grids were glow-discharged before use. Imaging was carried out at temperatures around 90 K. The TEM was operated at an acceleration voltage of 200 kV, and an objective lens defocus of about 1.5–2 μ m was used to

increase the contrast. Cryo-EM micrographs were recorded with a bottom-mounted 4.4k CMOS camera (TemCam-F416, TVIPS, Gauting, Germany). The total electron dose in each micrograph was kept below $20 e^-/\text{\AA}^2$.

XAS

To evaluate and compare the metal-coordination environments in different phases obtained through synthesis, XANES (near-edge x-ray absorption fine structure) and EXAFS (extended X-ray absorption fine-structure) spectroscopy measurements were performed at the BAMline (BESSY-II, Helmholtz Centre Berlin for Materials and Energy Berlin, Germany) [30].

XANES focusses on the pre-peak and absorption edge features. By analyzing this signal, the oxidation state, the nearest, first coordination sphere and even its degree of distortion can be determined. In contrast, the EXAFS region depicts the interaction of the scattered photoelectron on the surrounding atoms of the metal cation. Therefore, the local coordination environment of the surrounding atoms around the metal cation can be evaluated.

The beam was monochromatized using a Silicon double-crystal monochromator (DCM) with a crystallographic orientation of [111]. The size of the beam was 3 mm (l) x 1 mm (h). The measurements were performed at Co-K edge (7709 eV) and Ni-K edge (8333 eV) in transmission geometry, with two ionization chambers as detectors. The excitation energy was varied from 7606 eV to 8678 eV for Co and 8230 eV to 9302 eV for Ni, with varying energy steps. For the pre-edge region, the energy was varied in 10 eV steps; for the region around the edge, energy was tuned first in 0.5 eV steps, then in 1 eV steps and in the EXAFS region with a constant step in the k-space of 0.04 \AA^{-1} . The associated uncertainties were experimentally determined by measuring the cobalt and nickel metal foils, each 10 times. A value of ± 0.3 eV was obtained for both systems. For the measurement, the samples were mixed with boron nitride, placed in polycarbonate hole plates with a thickness of 1 mm and sealed with a polyimide tape (Kapton) on both sides. Before collecting the sample spectra, a cobalt or nickel foil was used as a reference for the respective K edge. The relative energies of the spectra were calibrated to the first inflection point from the first derivative of the cobalt/nickel metal absorption edge.

The resulting EXAFS data were processed by using ATHENA and ARTEMIS. Both programs belong to the main package IFEFFIT (v. 1.2.11) [31]. The respective Ni- and Co-phosphates phases were theoretically modelled and fitted to the measured spectra using Artemis. Pre-edge peak areas were determined by Gaussian function fitting and integration after baseline correction. All crystallographic structures were visualized with the software VESTA [32]

Results

The synthesis of transition metal struvites was optimized using different reaction conditions. The concentrations of the educt solutions (Mg^{2+} , Ni^{2+} and Co^{2+}) and initial pH values were varied to explore the phase stability field. Concentrations were chosen as they occur in several wastewater types.

Phase composition in the transition metal phosphate systems

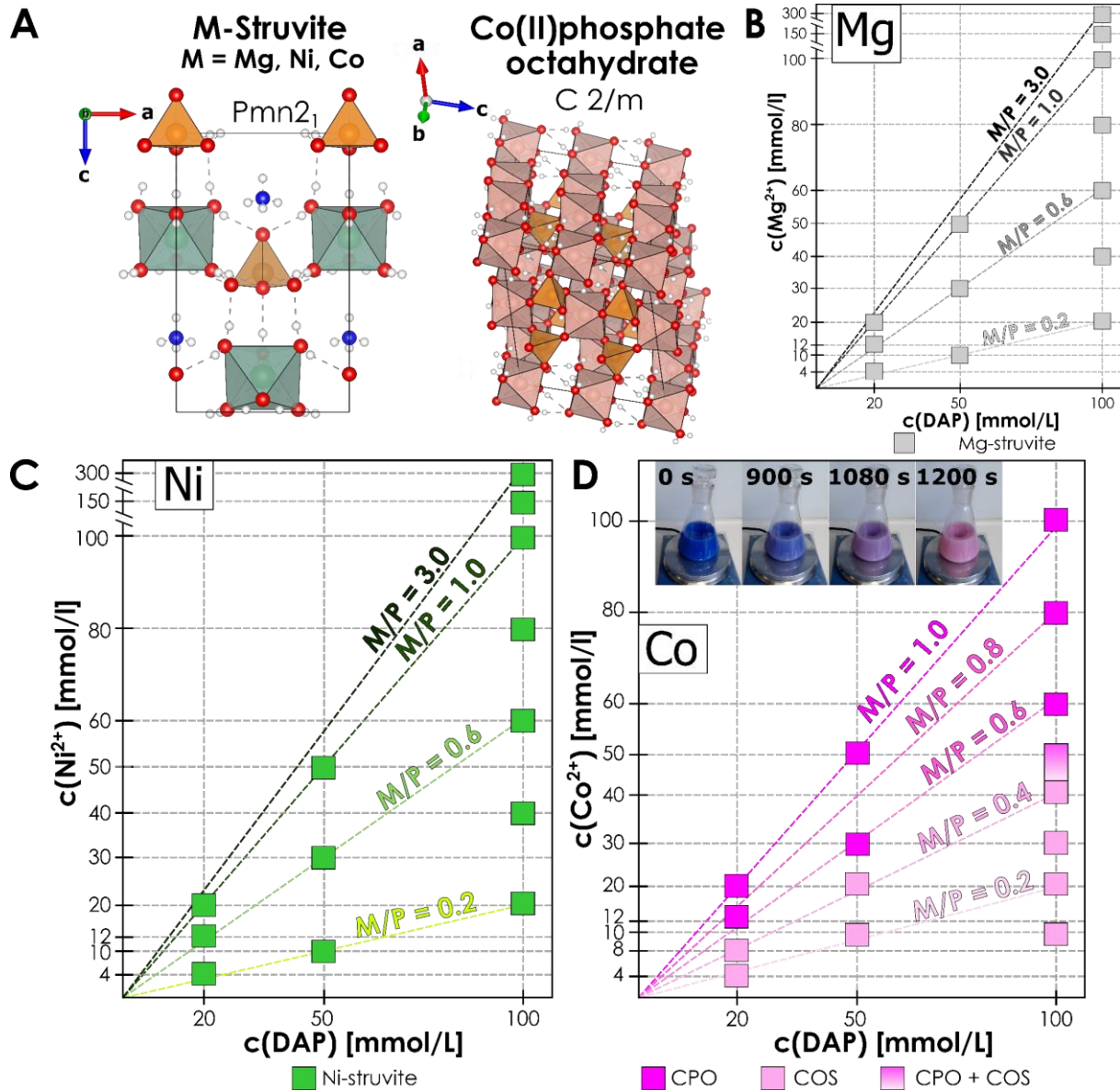


Figure 1A, B, C and D: Phase composition diagrams for Mg, Ni, and Co phosphates, which are derived from XRD data presented in the SI (see Fig. S1); (A) In the upper left corner the distinct crystallographic structure of M-struvite $\text{NH}_4\text{MPO}_4 \cdot 6\text{H}_2\text{O}$ (010) plane, M = Mg, Ni, Co and Co(II)phosphate octahydrate $\text{Co}_3(\text{PO}_4)_2 \cdot 8\text{H}_2\text{O}$ is displayed. For Mg (B) and Ni (C) systems, only struvite was observed. For Co (D) a color change of the aqueous solution from blue to purple to light pink at different times can be observed (see inset of Co-diagram). CPO: $\text{Co}_3(\text{PO}_4)_2 \cdot 8\text{H}_2\text{O}$ Cobalt(II)phosphate octahydrate, pakhomovskiyte; COS: $\text{NH}_4\text{CoPO}_4 \cdot 6\text{H}_2\text{O}$ Co-struvite. Crystal structure colors: white = hydrogen H, blue = nitrogen N, red = oxygen O; orange = phosphorous P; turquoise = metal M = Mg, Ni, Co; pink = cobalt Co; dotted lines hydrogen bonds

We explored the potential phase diagrams in the transition metal/DAP systems of M-struvites, M = Mg, Ni and Co (Fig. 1). The data points are derived from XRD measurements. At all concentration of Mg^{2+} , Ni^{2+} and all the different M/P ratios pure single-phase Mg or Ni-

struvites ($\text{NH}_4\text{MgPO}_4 \cdot 6\text{H}_2\text{O}$, $\text{NH}_4\text{NiPO}_4 \cdot 6\text{H}_2\text{O}$) are present (see Figure 1B and C). In the Co system at high DAP concentrations of 0.1 M only at a low $M/P < 0.4$, Co-struvite $\text{NH}_4\text{CoPO}_4 \cdot 6\text{H}_2\text{O}$ (ammoniumcobalt(II)phosphate hexahydrate, CoS) precipitated as a pure single phase (see Figure 1D). At higher $M/P > 0.5$, cobalt (II)phosphate octahydrate $\text{Co}_3(\text{PO}_4)_2 \cdot 8\text{H}_2\text{O}$ (CPO, Co-octahydrate) is formed as a single phase. In the intermediate interval $0.5 > M/P > 0.4$ a binary mixture of CPO and COS is formed (see Fig. S2A). At lower concentrations of DAP of 0.02 M the transition M/P ratio of Co-struvite and Co-octahydrate is slightly reduced to lower values below 0.4.

To evaluate how the initial pH impacts the phase stability of M-struvites, different amounts (1-10 ml) of 1 M $\text{NaOH}_{(\text{aq})}$ and 0.1 M $\text{H}_2\text{SO}_{4(\text{aq})}$ were added prior to mixing. In all pH samples $c(\text{M}^{2+}) = 0.02$ M and $c(\text{DAP}) = 0.1$ M was used to ensure in the phase stability field of M-struvite in all systems ($M = \text{Mg}^{2+}, \text{Ni}^{2+}, \text{Co}^{2+}$). For all initial pH adjusted samples and independent of the metal used, M-struvites formed as pure single phase (see Fig. S3A-F). We calculated the final equilibrium state of the solution based on the calculations with PHREEQC (see Table S2). The data from the pH-adjusted samples are included in the SI (see Fig. S1).

Evolution of the precipitation reaction

In both Ni and Mg systems the respective M-struvite formed as a pure single phase regardless of the reactant concentrations (see Figure 1, Mg and Ni). However, in the case of Co at concentrations of $c(\text{Co}^{2+}) > 0.4$ M with $c(\text{DAP}) = 0.1$ M other phases precipitated (see Figure 1, Co).

The phase diagrams in Figure 1 reflect only the final close-to-equilibrium outcome of the crystallization experiments. However, it must be further appended by the observations we made during our studies, which hint about the pathways by which the phases formed. The Co-struvite samples spontaneously dehydrated in air to Co-dittmarite $\text{NH}_4\text{CoPO}_4 \cdot \text{H}_2\text{O}$ (COD), as it was evidenced by XRD (ambient lab conditions, 1 to 3 days depending on a concentration 0.004 M ($t = 1$ d) to 0.4 M ($t = 3$ d)) and indicated by a color change from light purple to light pink. Therefore, Co-struvite had to be stored in the mother liquor for further analysis to prevent decomposition. After several minutes the cobalt phosphate phases transform from amorphous into crystalline which is accompanied by a color change from blue to purple to light pink. The time after which the transformation occurs is highly dependent on the stirring rate, temperature, pH, and concentration of the educts [26, 33, 34].

In the Ni-struvite system, we also observed a very short-living apparent colloidal precursor phase, while in Mg-struvite such early-stage transformations were absent within the observational window. A smooth color transition from a light green to an emerald green could be observed. All those observations point to complex crystallization pathways. They also indicate that the phenomena should be studied from the point of their evolution, and not only the final products, as we present further.

Due to the fact, that the precipitation processes involved the release of protons (see eq.[1] and [2]), we further followed the crystallization mechanisms by conducting time-resolved pH measurements. Here, pH was used as a time resolved proxy for evaluation of the reaction progress and kinetics.

Consequently, we followed the reaction progress, pH vs. time in equimolar high concentrated samples $c(\text{M})=c(\text{DAP})=0.1 \text{ M}$ and low concentrated samples $c(\text{M})=c(\text{DAP})=0.02 \text{ M}$ in the mixed solutions for 3600 s (see Figure 2).

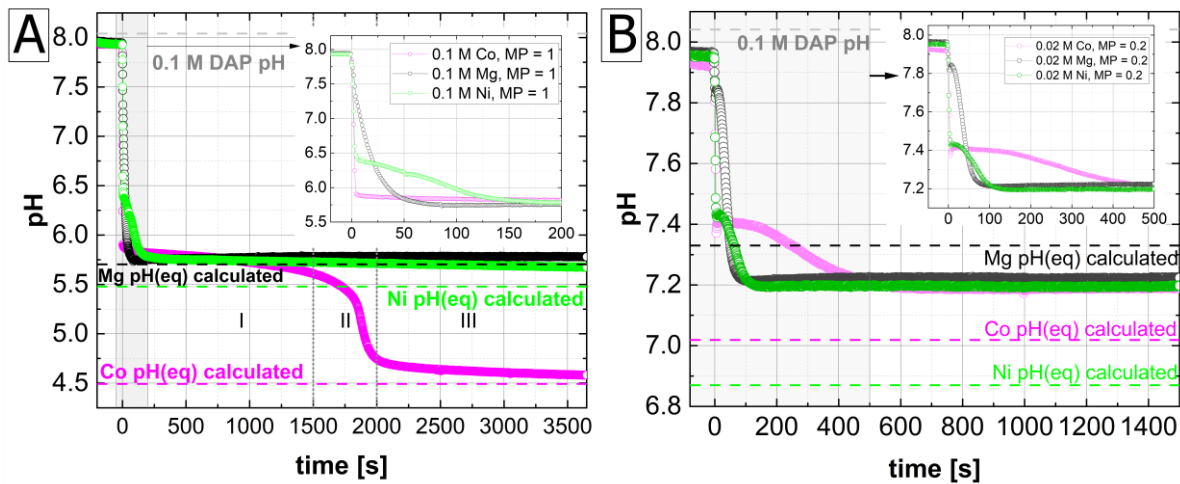


Figure 2: Time resolved pH measurements with 1 s resolution for 3600 s for the high concentrated samples (A) and the low concentrated samples (B); stage I, II, III indicate different slopes in the pH curve of the 0.1 M Co sample; in detail the pH evolution over the first 200s; the axes in the insets are the same as in the main graphs

The initial pH was $\sim 7.9-8.0$ for the 0.1 M DAP solution and ~ 5.7 for both NiSO_4 and CoSO_4 solutions at 0.1 M, and the 0.1 M MgCl_2 solution exhibited an initial pH of 7.0. When metal salt and DAP equimolar solutions were mixed, near-instant precipitation could be observed in both transition metal systems with the simultaneous drop in pH. On the other hand, the Mg-system had exhibited an induction time of $\sim 5 \text{ s}$ before it turned turbid. Immediately after mixing both 0.1 M solutions the pH dropped down to around ~ 5.8 for all systems. Here the color changed within seconds to white green for Ni and to white-blue/purple for Co. While the pH of the 0.1 M Mg sample declined slightly over the first 50-100 s (see Figure 1), the pH for 0.1 M Co reached nearly instantaneous a plateau value of 5.9 and sank slightly until around 1500 s, marked by phase I (see Figure 2A). After 1500 s a significant jump to a pH value of 4.6 over 500 s occurred in the 0.1 M Co sample marked by phases II and III which was most likely related to the transformation of the colloidal phases as the color changed simultaneously from purple to light pink here. The pH of the high concentrated Ni sample dropped first quick ($\approx 4 \text{ s}$) to 6.4 and declined over 150 s to 5.8. The Mg and Ni sample remained at their plateau value of 5.8 and sank barely.

As Co-struvite is only stable at low Co/P ratios ≤ 0.4 (see Figure 1C) additional pH measurements with a M/P ratio of 0.2 were conducted for all systems (see Figure 2). Here, the initial pH of the 0.02 M metal solutions was 6.5 (Mg), 5.9 (Ni and Co). The same 0.1 M DAP solution was used as before. Similar trends as in the high concentrated equimolar solution runs were observed except for Co. Here, the pH of the Co mixture declines slowly after 450 s to 7.2 and stagnated there like the other struvite samples. The PHREEQC equilibrium pH calculations are in a relatively close agreement with the experimental values with a confidence interval of approximated $\Delta\text{pH} \approx 0.3$ (see colored dotted lines in Figure 2). That indicates a progression of the precipitation reaction to completion in all samples. The deviation of the calculated and measured pH occurred probably due to the presence of amorphous phases

which are difficult to consider in the calculations as barely any (if any) thermodynamic data exist for them.

The Ni and Mg-struvite reaction proceeds fast within the first 100-150 s with no significant dependency of the concentration to reaction time while the Co-phosphate reactions exhibit much longer reaction times (400 s for 0.02 M and around 3000 s for 0.1 M Co^{2+}) due to the preservation and transformation of long-living colloidal phases. Therefore, as transitional colloidal phases effect majorly the kinetics of the precipitation reaction and crystallinity of the final products, it is necessary to investigate these transitional phases at least in the early stadium of nucleation. Especially from the aspect of crystallization engineering and mechanism it is questionable if in all these systems the final crystals formed on the same pathway as phosphates are known to include amorphous phases in the crystallization. [26, 34-37].

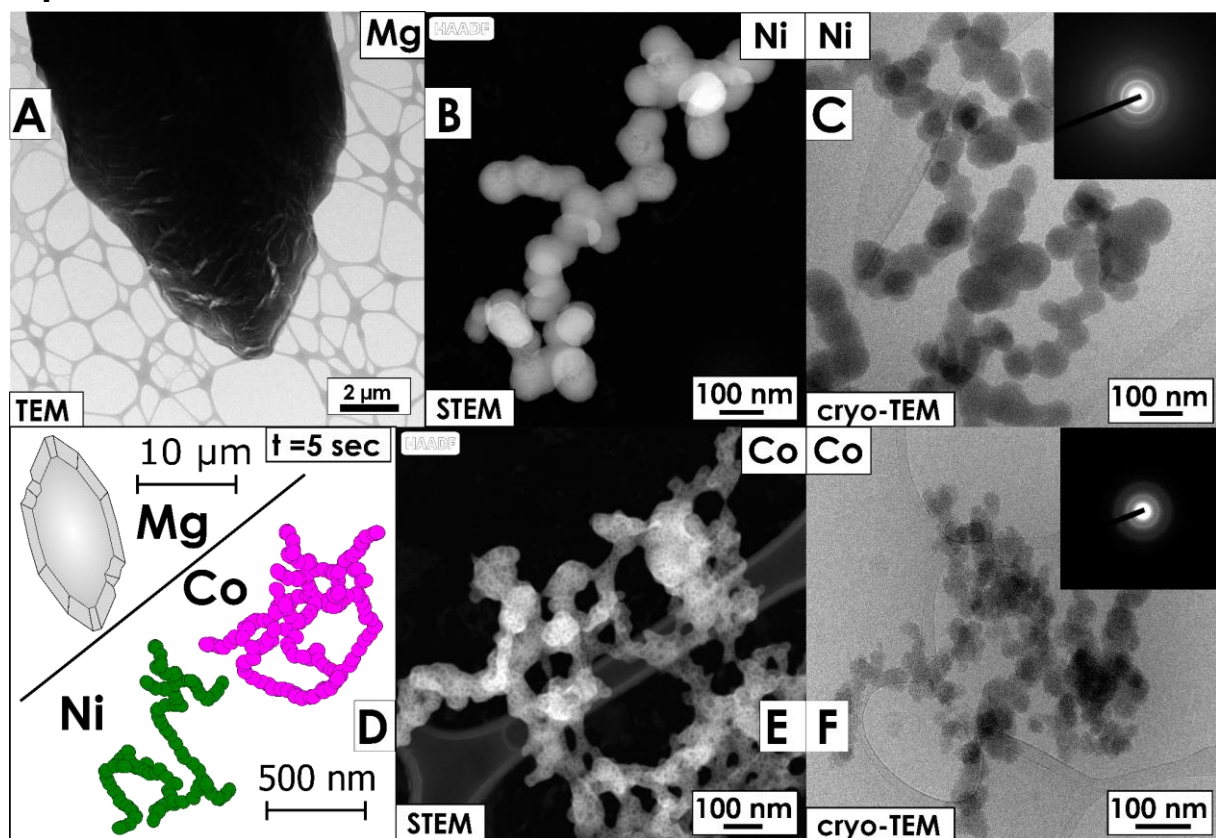


Figure 3A, B, C, D, E and F: Dry TEM image of immediately formed Mg-struvite crystal after 5 seconds of mixing (A) followed by dry STEM images of Ni and Co samples after 5 seconds mixing in high angular dark field = HAADF (B) and (E); On the right: cryo-TEM image of Ni and Co with SAED pattern (C) and (F); network of sphere shaped particles are clearly amorphous (SAED pattern); little sketch of the observed features in the upper left corner (D); EDS mappings and point measurements in the SI (see Fig. S4, S5 and S6)

Accordingly, to gain more insight into the formation of the transitional precursor phases during crystallization dry TEM and cryo-TEM measurements combined with EDS mappings and SAED analysis were performed on the samples. Each sample was prepared for a reaction time of 5 seconds (see Figure 3). The Mg sample shows immediately μm -sized big crystals of needle shaped Mg-struvite apparent to the eye with well-developed crystal planes (see Figure 3A and S4). In contrast to that the Ni- and Co-samples exhibit amorphous round nanoparticles with sizes of around 50 μm and chemical composition near to M-struvite which agglomerate to

bigger clusters (see Figure 3B, C, D, E, F, S5 and S6). The Ni-nanoparticles and their clusters appear more condensed and regular compared to those of Co.

Due to the fact transition metal struvites vary completely in their crystallization pathway from struvite (Mg-struvite) with different life spans of existing amorphous colloidal nanophases (Ni short-living nanophases for some seconds, cobalt long-living nanophases stable up to hours) an analysis of the crystalline precipitate could elucidate how these colloidal phases influence the crystalline particles. Different concentrations of M^{2+} /DAP and initial pH variations could influence the crystalline particles directly or on the amorphous nanophases indirectly which interact again with the crystals. Accordingly, this effect should be further investigated.

Crystal engineering of transition metal phosphates

To quantify how concentration changes of transition metal M^{2+} /DAP and initial pH effect the morphology and size of the crystallites, SEM analysis combined with EDX mappings was performed.

A strong dependency of the morphology and size of the crystals can be observed in the Ni-system in respect to the M/P ratio (see Figure 4A, S7). Ni-struvite morphologies with an M/P ratio ≥ 1 (high $c(Ni^{2+})$ compared to low $c(DAP)$) showed an anhedral rounded appearance and many agglomerated crystal nuclei with a crystallite size of (length from edge-to-edge) $11 \pm 3 \mu m$ with $c(Ni) = c(DAP) = 100 \text{ mM}$. At low M/P ratios ≤ 1 (low $c(Ni^{2+})$ compared to high $c(DAP)$) the crystals exhibited a more euhedral elongated X- or "coffin-like" shaped habit with crystallite size of $55 \pm 9 \mu m$ with $c(Ni) = 20 \text{ mM}$ and $c(DAP) = 100 \text{ mM}$. The X-shaped habit of the crystals occurred at low M/P ratios < 0.5 and high $c(DAP) \geq 50 \text{ mM}$ while the "coffin-like" morphology appeared at low M/P ratios < 0.5 but at low $c(DAP) \leq 50 \text{ mM}$. High Ni^{2+} concentrations at a constant DAP concentration favor many crystallites of smaller size with an anhedral appearance while high DAP concentrations at a constant Ni^{2+} concentration increase the crystallite size and idiomorphism of the crystallites. Adding $NaOH_{(aq)}$ and the coupled increase of pH favors the formation of M-struvite as protons are released through the precipitation reaction which counteracts the pH effect of OH^- ions (see eq.[1]). Adding $H_2SO_{4(aq)}$ and the coupled decrease of pH inhibits the precipitation of M-struvite as they decompose with lower pH and shifts the chemical equilibrium on the educt side (see eq.[1]). Adding $NaOH_{(aq)}$ to the Ni-struvite system alter the crystal morphology strongly and decreased the crystallite size from $50 \pm 9 \mu m$ to $5 \pm 1 \mu m$ (see grey inset in Figure 4A, S8). In addition, it changes the crystal habit to an orthorhombic prism appearance. Adding $H_2SO_{4(aq)}$ attacks the surface of the crystals strongly, although under these conditions the crystallite size and the X-shaped like morphology are not affected in comparison with the not pH adjusted sample with the same M^{2+} and DAP concentrations. All trends in terms of crystal morphology and size for Ni and Co are summarized in the SI (see Fig. S11A and B).

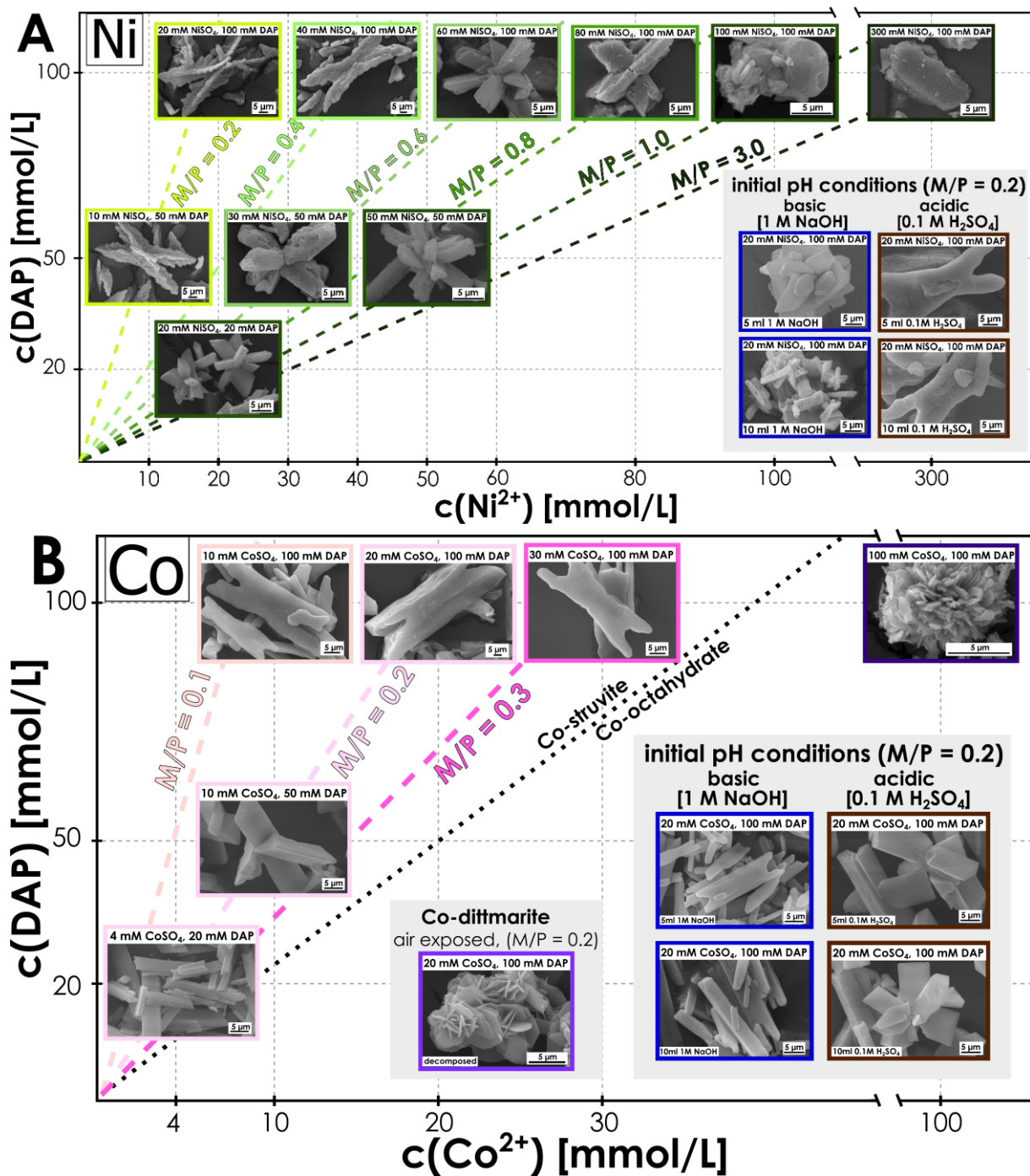


Figure 4A and B : $c(\text{M}^{2+})$ vs. $c(\text{DAP})$ plot with green (Ni, A)/pink(Co, B) color of frames and dotted lines indicating the distinct M/P ratio of the sample; lower right left corner: pH samples with a M/P ratio = 0.2 (0.02 M NiSO_4 / CoSO_4 , 0.1 M DAP) with different initial amounts of 1 M $\text{NaOH}_{(\text{aq})}$ (blue frames) or 0.1 M $\text{H}_2\text{SO}_{4(\text{aq})}$ (brown frames); in air decomposed Co-struvite to Co-dittmarite with a M/P ratio = 0.2 is displayed in the Co figure

Due to the limited stability of Co-struvite at low M/P ratios, only samples with a M/P ratio below 0.4 could be analyzed. Above a M/P ratio of 0.4 Co-octahydrate is stable. At a constant M/P ratio the crystallite size increased from $16 \pm 5 \mu\text{m}$ with 4 mM Co^{2+} and 20 mM DAP to $60 \pm 13 \mu\text{m}$ with 20 mM Co^{2+} and 100 mM DAP. The same but weaker following correlation as in the Ni-system could be observed. High DAP concentrations favor the formation of large euohedral crystals while higher Co^{2+} contents lead to small anhedral crystals. Similar to Ni-struvite, Co-struvite exhibits X-shaped crystal morphologies at high $c(\text{DAP}) \geq 50 \text{ mM}$ and low

M/P ratios < 0.3 , but the crystallographic planes are anhedrally developed (see Figure 4B, S9). The “coffin-like” habit occurs at low M/P ratios < 0.3 and low $c(\text{DAP}) \leq 50$ mM.

Co-octahydrate shows a rough 2D flake- or sheet-shaped morphology of the crystals and forms big crystal agglomerates of several μm . Co-dittmarite demonstrates a similar habit of regularly arranged 2D plates, also reported in other studies [33]. By increasing the pH with NaOH the crystal habit changed from a X-shaped morphology to elongated rod or prism-like habit (see Figure 4 Co, S10). Here the 5 ml 1 M $\text{NaOH}_{(\text{aq})}$ sample indicates remarkably the transition between those two morphologies. 10 ml $\text{NaOH}_{(\text{aq})}$ decreased the crystallite size from 60 ± 13 μm to 23 ± 6 μm . Reducing pH by addition of $\text{H}_2\text{SO}_{4(\text{aq})}$ favors the formation of tabular shaped Co-struvites with slightly decreased size of 35 ± 8 μm .

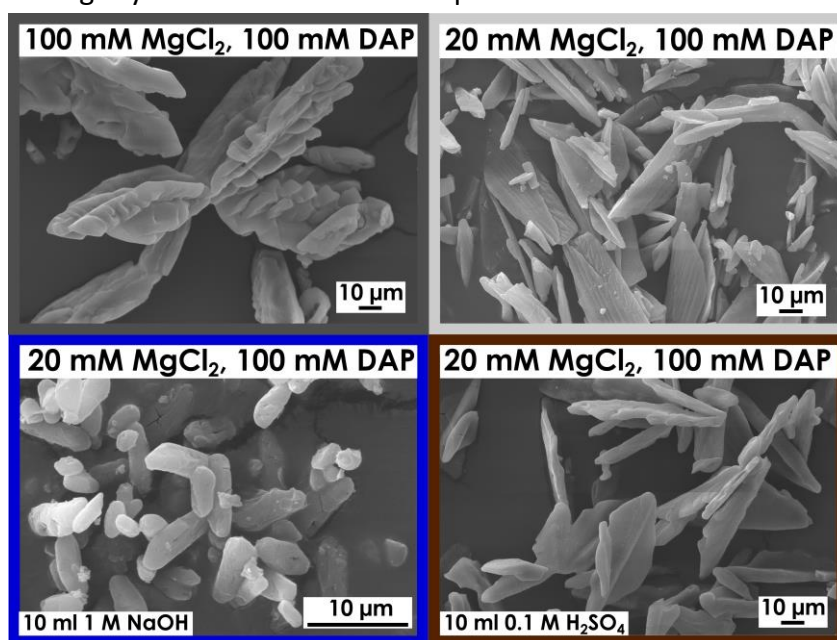


Figure 5: SEM images of different Mg-struvites at low M/P ratios of 0.2 with pH adjusted samples at the sides and one sample with high M/P ratio of 1

Highly investigated Mg struvites [27, 35, 38] were synthesized to serve as reference for transition metal phosphates (see Figure 5, S12). At high concentrations of DAP and Mg^{2+} struvite forms an X-shaped crystal habit with a crystallite size of 120 ± 20 μm while at low concentrations orthorhombic prisms occur and the crystallite size decreased to 40 ± 6 μm (see Figure 5, S12). In the case when we adjusted conditions to be initially acidic (adding 10 ml of 0.1 M H_2SO_4 with a pH = 1.00) the struvite crystals were comparable in terms of shape and size to those observed in pH unadjusted sample. However, the surface exhibited features of acidic leaching. Under basic conditions (adding 10 ml of 1 M $\text{NaOH}_{(\text{aq})}$ with a pH = 13.97), the size of the crystallites reduced to 5 ± 2 μm and the shape changed to more rounded orthorhombic prisms, but in contrast to acidic conditions the crystal surface were visually not affected.

These results already demonstrate a controllable and tunable adjustment of the crystallite size, morphology, and composition of M-struvites through changes in the reaction conditions. This property of capable crystal engineering makes them to promising candidates for waste water treatment and electrocatalysis.

Stability properties from the point of coordination environment

Crystalline M-struvites form in both transitional metal systems (Ni^{2+} , Co^{2+}), but they exhibit different stability. These differences can be explained in the context of the local coordination environment of the MO_6 octahedron in the struvite structure. Especially the dissimilarity between Ni- and Co-struvite is uncertain as both elements belong to the transition metals. To evaluate how the stability of Ni and Co phosphates is related to their coordination environment in the crystal structure and how they differ between each other, EXAFS measurements were performed on the powder samples.

In general, XAS analysis reveal quantitatively changes in oxidation state, in the local coordination geometry/symmetry and bond distances among the different Co- and Ni-phases. Especially the intensity of the pre-peak (XANES) which originates from the $1s-3d$ transitions expresses the degree of centrosymmetry and coordination environment in the vicinity of the considered ions (see Figure 6A and B, detailed window). As only $3d-4p$ hybridization enable parity allowed transitions the extent of those is strongly correlated with the coordination geometry. Near ideal octahedral coordination sites show very low pre-peak intensities due to the presence of an inversion center while more distorted geometries exhibit higher intensities.

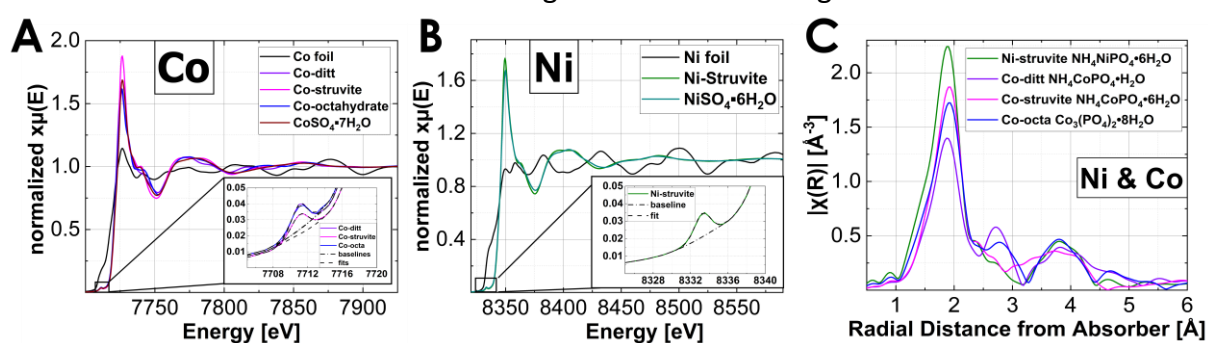


Figure 6A, B and C: XAS spectra of Co and Ni samples with detailed view of the pre-peak region; Fourier-transformed Ni- and Co spectra plotted in R-space with detailed view of XAS spectrum of Ni-struvite

Table 1: Pre-peak integration results by fitting gaussian functions with all fitting parameters

Sample	Prepeak area integration results			fit function: Gaussian			
	chemical formula	χ^2	R ² value	Pre-peak Area A_{pp} (err)	FWHM	Center	Max. Height
Co-octahydrate	$\text{Co}_3(\text{PO}_4)_2 \cdot 8\text{H}_2\text{O}$	5.03E-09	0.995	0.0363(4)	2.296	7711.2	0.0149
Co-dittmarite	$\text{NH}_4\text{CoPO}_4 \cdot \text{H}_2\text{O}$	5.04E-08	0.991	0.0355(4)	2.101	7711.5	0.0159
Co-struvite	$\text{NH}_4\text{CoPO}_4 \cdot 6\text{H}_2\text{O}$	3.66E-08	0.993	0.0298(3)	2.314	7711.1	0.0121
Ni-struvite	$\text{NH}_4\text{NiPO}_4 \cdot 6\text{H}_2\text{O}$	5.06E-09	0.992	0.0281(2)	1.969	8333.3	0.0134

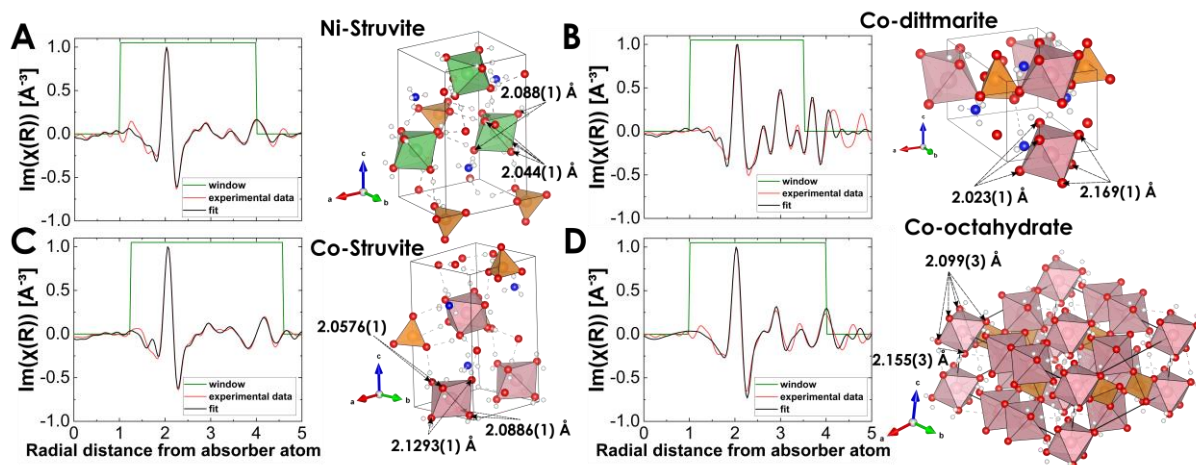


Figure 7A, B, C and D: Ni- and Co K-edge EXAFS data shown in real space for compound $\text{NH}_4\text{NiPO}_4 \cdot 6\text{H}_2\text{O}$ space group 31: $\text{Pmn}2_1$, $R = 0.005$ (A), for compound $\text{NH}_4\text{CoPO}_4 \cdot \text{H}_2\text{O}$ space group 31: $\text{Pmn}2_1$, $R = 0.008$ (B), for compound $\text{NH}_4\text{CoPO}_4 \cdot 6\text{H}_2\text{O}$ space group 31: $\text{Pmn}2_1$, $R = 0.012$ (C), and for compound $\text{Co}_3(\text{PO}_4)_2 \cdot 8\text{H}_2\text{O}$ space group 12: $C \frac{2}{m}$, $R = 0.005$ (D), experimental data: red, fit results: black; fit window: green.

The XAS spectra (Figure 6A and B) clearly prove that Co and Ni are exclusively present as the bivalent species in all samples by comparison with multiple M^{2+} standards (here only $\text{MSO}_4 \cdot n\text{H}_2\text{O}$ is shown for clarity). No indication for incorporated oxidized Ni^{3+} or Co^{3+} was observed in the powders. Quantitative pre-peak integration results are summarized in Table 1. Indicated by a minimal pre-peak area ($A_{\text{pp}} = 0.0298(3)$) and a maximized intensity in the white line Co-struvite as well as Ni-struvite ($A_{\text{pp}} = 0.0281(2)$) have a more centrosymmetric octahedral coordination environment compared to Co-dittmarite and Co-octahydrate ($A_{\text{pp}} = 0.0363(4)$ and $A_{\text{pp}} = 0.0355(4)$). After FT of $\chi(k)$ into R-space radial distances from the absorber atom can be observed (see Figure 6C). At around $R \approx 1.9 \text{ \AA}$ all samples show a maximum which is related to the degeneracy of single scattering path of the Ni-O or Co-O bond length. In the case of single scattering, we have a direct measure of the coordination number (CN). The peak at $R \approx 2.7 \text{ \AA}$ in CPO and CoD fits to the Co-P single scattering path, which is absent in the M-struvites. In CPO and CoD the CoO_6 octahedrons are linked to four (CPO) or five (CoD) O^{2-} of PO_4 tetrahedrons (short distance of Co-P) while in the struvite structure they are coordinated by the O^{2-} of six water molecules, and therefore are isolated from the phosphate tetrahedron (long distance of Ni-P and Co-P, see Fig. S13). The slight color change between CoS, CoD and CPO of the chemical compounds of Co is probably related to how much of the ligands are crystal water, six for CoS, five for CoD and four for CPO. The peak at $R \approx 3.8 \text{ \AA}$ consists of several single and multiple scattering paths such as Co-N, Co-H, Co-P, Co-O-O.

Quantitative real-space fittings on the radial distribution function reveal the bond distances in the first coordination environment around the Co^{2+} and Ni^{2+} metal cation. All fitting parameters are shown in Table S3, S4, S5 and S6. By calculating the mean bond distance and its sphere volume, a quantitative comparison of the coordination sphere is possible. The M-struvites (M-struvite Ni: $2.059(6) \text{ \AA}$ Co: $2.091(1) \text{ \AA}$) demonstrate slightly lower mean bond distances than CoD and CPO (CoD: $2.096(1) \text{ \AA}$, CPO: $2.11(2) \text{ \AA}$). The fitted bond distances are

visualized with the calculated fits in Figure 7 for the different compounds (see Table S3, S4, S5 and S6).

Discussion

In all chemical systems crystalline M-struvite could be obtained. The nucleation pathways to the final crystal vary between the chemical systems. At concentrations of 0.02 M Mg, Ni, and Co form single phase M-struvite. Here the ammonium ion is bound in the precipitates. The reduction of the pH represents a combination of mixing a slightly acidic solution to the mixture and the released protons from precipitation reaction of M-struvite. At concentrations of 0.1 M Co and 0.1 M DAP, CPO is forming through transformation of amorphous phases accompanied by a color change from blue to purple to pink. This transition of colors is highly significant because it points to specific meta-stable reactions. In CPO the M/P ratio in CPO is 3:2 which leads to remaining amounts of PO_4^{3-} and NH_4^+ in the aqueous solution due to the absence of M-struvites (M/P ratio of 1:1). As ammonium is the most abundant species in the aqueous solution, the dissociation equilibrium to ammonia with the release of protons dominates the pH. The remaining less abundant phosphate and the coupled dissociation to $\text{H}_x\text{PO}_4^{3-x}$ species with the removal of protons can only compensate to a limited amount. It is assumed the jump of the pH after 1800 s is related partly to the transformation of the amorphous Co phases to crystalline CPO with the release of protons as the color changes from purple to pink in this time interval. Moreover, one should also consider the formation of $\text{Co}(\text{NH}_3)_x\text{H}_2\text{O}_{6-x}^{2+}$ aqua complexes due to the non-complete consumption of Co^{2+} with the additional reduction of the pH through proton release by converting ammonium to ammonia. The light pink color of the residual solution after the precipitation of CPO was an indicator for this assumption [39, 40]. The 0.1 M concentrated Ni and Mg samples mixed with 0.1 M DAP exhibit no late reduction of pH as most of the ammonium is bound in the struvites and probably no amorphous metal phosphate phase is stable over a long period (> mins). In general, the morphology of the crystals observed in SEM is influenced by vacuum indicated by intermittent vacuum-induced cracks. Nevertheless, since all crystals are exposed to the same vacuum influence, the change in morphology should be related to the differences in the experimental conditions. Looking at the ionic radii of $\text{Co}^{2+[\text{VI}]}$ (0.75 Å, high state) and $\text{Ni}^{2+[\text{VI}]}$ (0.69 Å) compared to $\text{Mg}^{2+[\text{VI}]}$ (0.72 Å), all ions have similar radii so they could be potentially substituted one for another in the struvite structure $\text{Pm}\bar{n}2_1$. Looking on the formation of the crystals, a higher supersaturation leads to a higher nucleation rate which provides many crystal nuclei of smaller crystallite size. At low supersaturations only a few crystal nuclei grow significantly due to a lower nucleation rate. Based on observations, the Ni^{2+} and Co^{2+} concentration effects the struvite morphology as a regulator of supersaturation and reaction kinetics but also as the source for potential metal aqua complexes, which in turn influence the precipitation through a positive feedback loop. Higher concentrations of DAP correlate with the apparent elongation and increasing crystallite size of the crystals at a constant M/P ratio. Similar effects were observed in the crystallization of Mg-struvites [38]. As in DAP two moles of NH_4^+ are present, the effect of higher DAP concentrations on the crystals is mostly related to higher concentrations of ammonium.

In all systems a reduction of the initial pH by adding $\text{NaOH}_{(\text{aq})}$ decreased the crystallite size significantly and stabilized a more rod/prism like morphology of the crystals. By adding $\text{H}_2\text{SO}_{4(\text{aq})}$ the crystallite size remained practically unchanged in the Ni-system, but the crystal surface was clearly affected by the acid. In the Co-system the crystallite size decreased slightly around 10 μm and the morphology changed to more tabular shapes. The Co-samples treated with sulfuric acid exhibited a short presence of the transitional amorphous colloidal phases of 10-15 mins as well as they decomposed faster to Co-dittmarite in several hours compared to the pH unaffected samples. Here again, Co-struvite demonstrates a low stability compared to Ni-struvite. As only 0.1 M $\text{H}_2\text{SO}_{4(\text{aq})}$ was added initially not to dissolve the crystals completely, the absolute change in pH $|\Delta\text{pH}|$ was lower than the one induced by adding higher concentrated 1 M $\text{NaOH}_{(\text{aq})}$ to the system. As an increase of the pH (i.e. decrease in proton concentration) shifts the equilibrium to the side of the products in eq.[1], a high number of crystal nuclei are formed which grow simultaneously. Consequently, as many crystals of a low size have a higher surface area compared to a few crystals with a big size, these nuclei will grow only to a limited extent. Therefore, these crystals are much smaller than in the not pH adjusted runs where only few crystals grew large. Low concentrated sulfuric acid already reduces the life span of the transitional colloidal nanophases and the final crystalline Co-struvite significantly. From the point of view of saturation index (SI) and ion activity product (IAP), an initial basic pH increases the $\text{SI}_{\text{M-struvite}}$ as the activity of $[\text{PO}_4^{3-}(\text{aq})]$ increases. However, this shift of the equilibrium to the product side is limited to a certain pH, because at a high pH (for Mg-struvite pH = 11) the presence of $\text{NH}_3^0(\text{aq})$ and $\text{M}(\text{OH})^-(\text{aq})$ species reduces the activities of $\text{NH}_4^+(\text{aq})$ and M^{2+} and therefore compensates the increase of $a(\text{PO}_4^{3-}(\text{aq}))$ [38].

Other 3d ions like Zn^{2+} , Cu^{2+} or Fe^{2+} which tend to form amorphous and/or other crystalline phases could be potentially precipitated as M-struvite as soon as low amounts of Ni or Co are added. In such a way 3d-metals which are favorized in the M-struvite structure can stabilize other misfitting 3d-metals in the struvite structure. As in waste waters multiple metal cations are present, an increase of a struvite "fitting" element like Ni could lead to a precipitation of struvite solid solution between all these 3d metals. Nevertheless, Co-struvite demonstrates a low stability compared to Ni-struvite as it decomposes to Co-dittmarite in air or is replaced at higher concentrations of $c(\text{Co}^{2+}) > 0.4$ by CPO as the most stable phase. Hints on these stability properties are hidden in the metal coordination environment.

The CoO_6 octahedron in the struvite structure shows a higher degree of distortion compared to NiO_6 in Ni-struvite but a lower one compared to the other Co-phases (see pre-peak area fits in Table 1). According to that the distortion of the CoO_6 octahedron as well as the configuration of three different bond distances with low degeneracies of two (see Figure 7) may not be favorable for the struvite structure. The volume and the distortion of the CoO_6 octahedron could expand the stability of the M-struvite structure and therefore, it tends to decompose to Co-dittmarite. Here, the Co-dittmarite structure allows a more distorted coordination environment of the central metal cation since it is coordinated by five corner-linking O^{2-} anions of the phosphate tetrahedrons and one O^{2-} anion from the remaining crystal water (see Fig. S13). Indicators for this assumption is the high stability of Co(II)phosphate octahydrate at high M/P ratios > 0.4 (see Figure 1 and Figure 4B) where Co^{2+} is also bonded in

a similar distorted octahedral coordination as in Co-dittmarite by two corner linking O^{2-} anions of the phosphate tetrahedrons and four O^{2-} anions from the crystal water (see Fig. S13). As H_2O behaves for most of the bivalent transition metal ions as a weak field ligand, the high spin configuration is realized in their complexes. Looking on the Irving-Williams thermodynamic series of high spin first row transition metals in the bivalent oxidation state the stability of metal complexes decreases in the order $Mn^{2+} < Fe^{2+} < Co^{2+} < Ni^{2+} < Cu^{2+} > Zn^{2+}$ indifferent from the type of ligand coordinates [41, 42]. Co^{2+} as a d^7 ion shows a strong Jahn-Teller effect in octahedral coordination with weak ligands like H_2O (high state) compared to Ni^{2+} with a d^8 orbitals as more unpaired electrons occur in this electron configuration. In agreement with our results other studies demonstrated a distorted non-centrosymmetric octahedral coordination of Co^{2+} as d^7 ion in Co-doped Ni-struvite while Ni^{2+} as a d^8 ion exhibits a near ideal cubic octahedral coordination based on electron spin resonance spectroscopy [43]. Therefore, we suggest that the different stabilities of Ni- and Co-struvite are mainly influenced by the electronical d-configuration and their ionic radii for the struvite structure $Pmn2_1$.

Interestingly, struvite and Ni-struvite seem to have a higher stability compared to Co-struvite as no other phases precipitate and no decomposition to other phases could be observed.

The strong similarities between Ni- and Mg- struvite is probably related to the comparable solubility and the absence of long-living metastable amorphous phases. From dry TEM and cryo-TEM measurements combined with SAED patterns we have no indicator found for an amorphous phase in the Mg-system as the crystals grew immediately after mixing to μm size (see Figure 3B, 3E, Fig. S4). In contrast, short-living amorphous nanophases occurred in the Ni-system which form in the early stages of precipitation within seconds. These regular amorphous nanoclusters of spherical particles probably aggregate and condensate with higher reaction times to a precursor unit of a crystal.

The Co-system demonstrates metastable long-living (minutes to hours) amorphous phases on the way to the final crystalline Co-struvite with a related color change from purple to light pink. Here, the Co^{2+} changes its configuration from tetrahedral to octahedral coordination which leads to a slightly different color absorption [33, 34]. Similar to the Ni-samples, cobalt forms amorphous round nanoparticles (see Figure 3, Fig. S6). The condensation and densification to a proto crystalline unit takes place in a longer time period (mins to hours) than in the Ni-system. Indicators for this theory are the pH curves at high and low concentrations and the associated color change of the aqueous solution. It may explain why a weak correlation between concentration of Co^{2+}/DAP and crystal habit can be observed compared to Ni and Mg. The transitional nanophases of Co impact the influence of the educts on the crystallization. Based on the crystallization of M-struvites follows a non-classical nucleation pathway [44, 45] which involves transitional amorphous precursor phases on the way to the final crystalline product (see Figure 8). Here, amorphous colloidal nanoparticles form within seconds which aggregate and transform within minutes of reaction time. These aggregates condensate to a proto-crystalline nucleus which facilitate the next crystallisation of new nuclei through providing of interfaces. In the final step depending on the reaction conditions these crystal nuclei develop different morphologies and sizes.

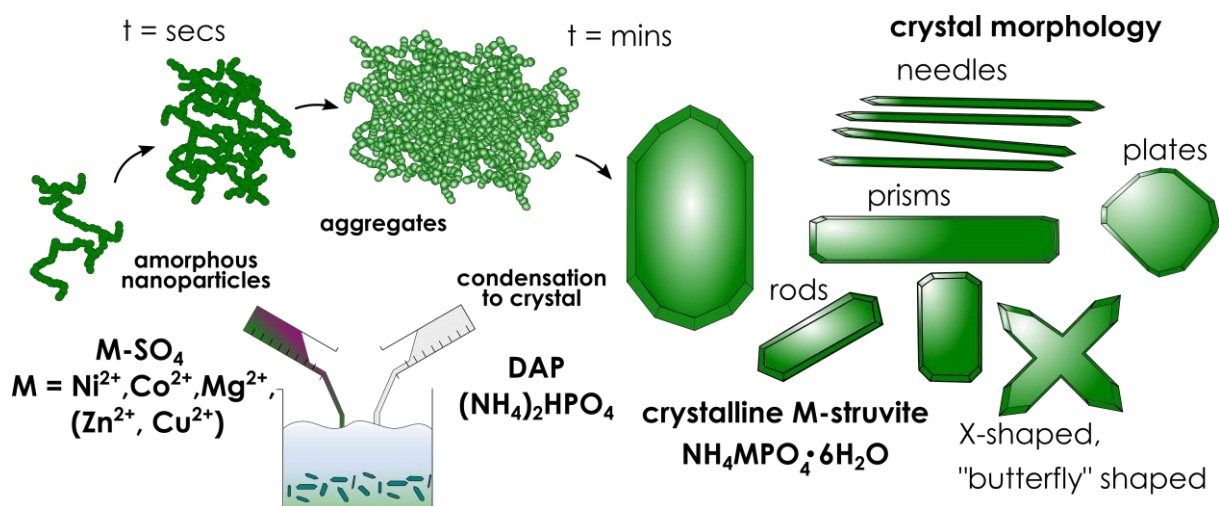


Figure 8: Sketch of the formation of different transition metal struvite crystals through a non-classical crystallization theory including amorphous nanoclusters.

Conclusion

Our investigation of transition metal struvites as potential systems for multicomponent coprecipitation led to different crucial insights. Ni-struvite is stable in multiple concentrations of the educts and at different metal/phosphate (M/P) ratios. Co-struvite precipitates at a M/P ratio of 0.4, whereas above this value Co(II)-phosphate octahydrate is stable. Ni- and Co struvites form amorphous precursor phases on the way to the final crystalline product while no nanophase was observed for Mg. Control of different morphologies and sizes of transition metal struvite can be obtained depending on the crystallization conditions.

Transition metal phosphates appear to form through a non-classical nucleation pathway, which involves multiple amorphous nanophases during precipitation. Due to the low solubility product and their controlled precipitation through adjusting the reaction conditions transition metal struvite is a promising recovery material for extracting NH₄⁺, PO₄³⁻ and heavy metals at simultaneously out of agricultural and mine waste waters. Furthermore, the possibility to specifically set/tune the morphology and properties opens the prospect of preparing materials directly tailored for the planned electrochemical application.

Acknowledgements

We acknowledge Uwe Reinholz, Martin Radtke and Kirill Yusenko for their support in the XAS measurements at the BAMline beamline of BESSY II. We acknowledge BAM and Helmholtz-Zentrum Berlin (HZB) for providing us with the beamtime at BESSY II. We thank Carsten Prinz for TEM measurements.

References

- [1] Cordell D., Drangert J.-O., White S. The story of phosphorus: Global food security and food for thought. *Global Environmental Change*. 2009;19(2):292-305.
- [2] Filippelli G.M. The Global Phosphorus Cycle. *Reviews in Mineralogy and Geochemistry*. 2002;48(1):391-425.
- [3] Gislev M., Grohol M., Mathieux F., Ardente F. Report on Critical Raw Materials in the Circular Economy. European Commission; 2018.
- [4] Neset T.S., Cordell D. Global phosphorus scarcity: identifying synergies for a sustainable future. *J Sci Food Agric*. 2012;92(1):2-6.
- [5] Hallas J., Mackowiak C., Wilkie A., Harris W. Struvite Phosphorus Recovery from Aerobically Digested Municipal Wastewater. *Sustainability*. 2019;11(2).
- [6] Prot T., Korving L., Dugulan A.I., Goubitz K., van Loosdrecht M.C.M. Vivianite scaling in wastewater treatment plants: Occurrence, formation mechanisms and mitigation solutions. *Water Res*. 2021;197:117045.
- [7] Le Corre K.S., Valsami-Jones E., Hobbs P., Parsons S.A. Phosphorus Recovery from Wastewater by Struvite Crystallization: A Review. *Critical Reviews in Environmental Science and Technology*. 2009;39(6):433-77.
- [8] Uysal A., Yilmazel Y.D., Demirer G.N. The determination of fertilizer quality of the formed struvite from effluent of a sewage sludge anaerobic digester. *J Hazard Mater*. 2010;181(1-3):248-54.
- [9] Hao X., Wang C., van Loosdrecht M.C., Hu Y. Looking beyond struvite for P-recovery. *Environ Sci Technol*. 2013;47(10):4965-6.
- [10] Sena M., Seib M., Noguera D.R., Hicks A. Environmental impacts of phosphorus recovery through struvite precipitation in wastewater treatment. *Journal of Cleaner Production*. 2021;280.
- [11] Zhao H., Yuan Z.Y. Insights into Transition Metal Phosphate Materials for Efficient Electrocatalysis. *ChemCatChem*. 2020;12(15):3797-810.
- [12] Lin R., Ding Y. A Review on the Synthesis and Applications of Mesostructured Transition Metal Phosphates. *Materials (Basel)*. 2013;6(1):217-43.
- [13] Xu X., Du P., Guo T., Zhao B., Wang H., Huang M. In situ Grown Ni phosphate@Ni₁₂P₅ Nanorod Arrays as a Unique Core–Shell Architecture: Competitive Bifunctional Electrocatalysts for Urea Electrolysis at Large Current Densities. *ACS Sustainable Chemistry & Engineering*. 2020;8(19):7463-71.
- [14] Meguerdichian A.G., Jafari T., Shakil M.R., Miao R., Achola L.A., Macharia J., et al. Synthesis and Electrocatalytic Activity of Ammonium Nickel Phosphate, [NH₄]NiPO₄·6H₂O, and beta-Nickel Pyrophosphate, beta-Ni₂P₂O₇: Catalysts for Electrocatalytic Decomposition of Urea. *Inorg Chem*. 2018;57(4):1815-23.
- [15] Huang H., Xu C., Zhang W. Removal of nutrients from piggery wastewater using struvite precipitation and pyrogenation technology. *Bioresour Technol*. 2011;102(3):2523-8.
- [16] El Diwani G., El Rafie S., El Ibiari N.N., El-Aila H.I. Recovery of ammonia nitrogen from industrial wastewater treatment as struvite slow releasing fertilizer. *Desalination*. 2007;214(1-3):200-14.
- [17] Münch E.V., Barr K. Controlled struvite crystallisation for removing phosphorus from anaerobic digester sidestreams. *Water Research*. 2001;35(1):151-9.
- [18] Zhangchen R.L., W.; Guan, Q.; Ji, H.; Li, Y.; Zhang, J.; Song, J.; Zhong, Y.; Zhou, L. Struvite as seed materials for treatment of heavy metals in wastewater. *IOP Conference Series: Earth and Environmental Science (EES)*. 2021;770:1-5.

- [19] Rouff A.A. Sorption of chromium with struvite during phosphorus recovery. *Environ Sci Technol.* 2012;46(22):12493-501.
- [20] Rouff A.A., Juarez K.M. Zinc interaction with struvite during and after mineral formation. *Environ Sci Technol.* 2014;48(11):6342-9.
- [21] Lu X., Huang Z., Liang Z., Li Z., Yang J., Wang Y., et al. Co-precipitation of Cu and Zn in precipitation of struvite. *Sci Total Environ.* 2021;764:144269.
- [22] Lin J., Chen N., Pan Y. Arsenic incorporation in synthetic struvite (NH₄MgPO₄·6H₂O): a synchrotron XAS and single-crystal EPR study. *Environ Sci Technol.* 2013;47(22):12728-35.
- [23] Ravikumar R.C., AV.; Rama Krishnar, CH.; Reddy, YP. X-ray powder diffraction, thermal analysis and IR studies of zinc ammonium phosphate hexahydrate. *Optoelectronics and Advanced Materials -Rapid Communciations.* 2010;4:215-9.
- [24] Abbona F.A.-F., M.; Croni Bono, C.; Lundager Madsen, HE. Effect of ammonia excess on the crystal habit of NiNH₄PO₄·6H₂O (Ni-struvite). *Journal of Crystal Growth.* 1994;143:256-60.
- [25] Haferburg G., Kloess G., Schmitz W., Kothe E. "Ni-struvite" - a new biomineral formed by a nickel resistant *Streptomyces acidiscabies*. *Chemosphere.* 2008;72(3):517-23.
- [26] Hövelmann J., Stawski T.M., Freeman H.M., Besselink R., Mayanna S., Perez J.P.H., et al. Struvite Crystallisation and the Effect of Co²⁺ Ions. *Minerals.* 2019;9(9).
- [27] Hövelmann J., Stawski T.M., Besselink R., Freeman H.M., Dietmann K.M., Mayanna S., et al. A template-free and low temperature method for the synthesis of mesoporous magnesium phosphate with uniform pore structure and high surface area. *Nanoscale.* 2019;11(14):6939-51.
- [28] Parkhurst D.L., Appelo C.A.J. Description of input and examples for PHREEQC version 3: a computer program for speciation, batch-reaction, one-dimensional transport, and inverse geochemical calculations. Reston, VA: U.S. Geological Survey; 2013.
- [29] Madsen H.E.L. Solubility Product of Ni-Struvite, NH₄NiPO₄·6H₂O, at 25°C. *Advances in Chemical Engineering and Science.* 2017;07(02):206-14.
- [30] Görner W., Hentschel M.P., Müller B.R., Riesemeier H., Krumrey M., Ulm G., et al. BAMline: the first hard X-ray beamline at BESSY II. *Nuclear Instruments and Methods in Physics Research A.* 2001;467-468:703-6.
- [31] Ravel B., Newville M. ATHENA, ARTEMIS, HEPHAESTUS: data analysis for X-ray absorption spectroscopy using IFFFIT. *J Synchrotron Radiat.* 2005;12(Pt 4):537-41.
- [32] Momma K., Izumi F. VESTA: a three-dimensional visualization system for electronic and structural analysis. *Journal of Applied Crystallography.* 2008;41(3):653-8.
- [33] Bach S., Visnow E., Panthöfer M., Gorelik T., Buzanich A.G., Gurlo A., et al. Hydrate Networks under Mechanical Stress - A Case Study for Co₃(PO₄)₂·8H₂O. *European Journal of Inorganic Chemistry.* 2016;2016(13-14):2072-81.
- [34] Bach S., Panthöfer M., Bienert R., Buzanich A.d.O.G., Emmerling F., Tremel W. Role of Water During Crystallization of Amorphous Cobalt Phosphate Nanoparticles. *Crystal Growth & Design.* 2016;16(8):4232-9.
- [35] Crutchik D., Garrido J.M. Struvite crystallization versus amorphous magnesium and calcium phosphate precipitation during the treatment of a saline industrial wastewater. *Water Sci Technol.* 2011;64(12):2460-7.
- [36] Zhang Q., Jiang Y., Gou B.-D., Huang J., Gao Y.-X., Zhao J.-T., et al. In Situ Detection of Calcium Phosphate Clusters in Solution and Wet Amorphous Phase by Synchrotron X-ray Absorption Near-Edge Spectroscopy at Calcium K-Edge. *Crystal Growth & Design.* 2015;15(5):2204-10.

- [37] Mahamid J., Sharir A., Weiner S. Amorphous calcium phosphate is a major component of the forming fin bones of zebrafish: Indications for an amorphous precursor phase. *PNAS* 2008;105:12748-53.
- [38] Shaddel S., Ucar S., Andreassen J.P., Osterhus S.W. Enhancing efficiency and economics of phosphorus recovery process by customizing the product based on sidestream characteristics - an alternative phosphorus recovery strategy. *Water Sci Technol.* 2019;79(9):1777-89.
- [39] Blyholder G., Ford N. Far-Infrared Spectra of Some Mono- and Polynuclear Aqua-Substituted cobalt-Ammine Complexes. *The Journal of Physical Chemistry.* 1964.
- [40] Schmiedekamp A.M., Ryan M.D., Deeth R.J. Six-Coordinate Co^{2+} with H_2O and NH_3 Ligands: Which Spin State Is More Stable? *Inorganic Chemistry.* 2002;41:5733-43.
- [41] Irving H., Williams R. Order of stability of metal complexes. *Nature.* 1948;162.
- [42] Irving H., Williams R. The stability of transition-metal complexes. *J Chem Soc.* 1953:3192-210.
- [43] Foglio M.B., G. Study of Co^{2+} in Different Crystal Field Environments. *Brazilian Journal of Physics.* 2005;36:40-54.
- [44] De Yoreo J. Crystal nucleation: more than one pathway. *Nat Mater.* 2013;12(4):284-5.
- [45] Andreassen J.-P., Lewis A.E. Classical and Nonclassical Theories of Crystal Growth. *New Perspectives on Mineral Nucleation and Growth* 2017. p. 137-54.

Supporting Information

List of Figure

Figure 1A-E: XRD patterns Mg, Ni and Co.....	3
Figure 2A and B: additional XRD patterns of Co	4
Figure 3A-F: XRD patterns of pH adjusted samples	5
Figure 4 conventional TEM images of Mg sample	7
Figure 5: conventional STEM analysis of Ni sample after t = 5 sec mixing	8
Figure 6: conventional STEM analysis of Co sample after t = 5 sec mixing.....	9
Figure 7A-J: SEM images of Ni- struvite	11
Figure 8A-D: SEM images of pH adjusted Ni-samples	11
Figure 9A-G: SEM images of Co phosphate phases.....	12
Figure 10A-D: SEM images of pH adjusted Co-samples.....	13
Figure 11A and B: Crystallization trends in th Ni and Co system.	14
Figure 12A-D: SEM images of Mg-struvite.....	15
Figure 13: Crystallographic differences between the Co-phosphate phases.....	16

List of Tables

Table 1: detailed reaction conditions of the precipitated samples.....	2
Table 2: PHREEQC calculations of pH change in the solution,	6
Table 3: Artemis fit parameter for Ni-struvite	17
Table 4: Artemis fit parameter for Co-struvite	18
Table 5: Artemis fit parameter for Co-dittmarite (COD)	19
Table 6: Artemis fit parameter for Co-phosphate octahydrate (CPO).....	20
Table 7: concentrations of Ni, Co, NH ₄ and P in waste waters	22

Table 1: detailed reaction conditions of the precipitated samples in 200 ml reaction volume with 100 ml of each, metal salt and DAP;

c(NiSO₄)	c(DAP)	M/P ratio	c(CoSO₄)	c(DAP)	M/P ratio	c(MgCl₂)	c(DAP)	M/P ratio
[M]	[M]		[M]	[M]		[M]	[M]	
0.004	0.02	0.2	0.004	0.02	0.2	0.004	0.02	0.2
0.01	0.05	0.2	0.008	0.02	0.4	0.01	0.05	0.2
0.012	0.02	0.6	0.01	0.05	0.2	0.012	0.02	0.6
0.02	0.02	1	0.012	0.02	0.6	0.02	0.02	1
0.02	0.1	0.2	0.02	0.02	1	0.02	0.1	0.2
0.03	0.05	0.6	0.02	0.1	0.2	0.03	0.05	0.6
0.04	0.1	0.4	0.03	0.05	0.6	0.04	0.1	0.4
0.05	0.05	1	0.04	0.1	0.4	0.05	0.05	1
0.06	0.1	0.6	0.042	0.1	0.42	0.06	0.1	0.6
0.08	0.1	0.8	0.046	0.1	0.46	0.08	0.1	0.8
0.1	0.1	1	0.05	0.05	1	0.1	0.1	1
0.15	0.1	1.5	0.05	0.1	0.5	0.15	0.1	1.5
0.3	0.1	3	0.054	0.1	0.54	0.3	0.1	3
			0.058	0.1	0.58			
			0.06	0.1	0.6			
			0.08	0.1	0.8			
			0.1	0.1	1			
			0.15	0.1	1.5			
			0.3	0.1	3			

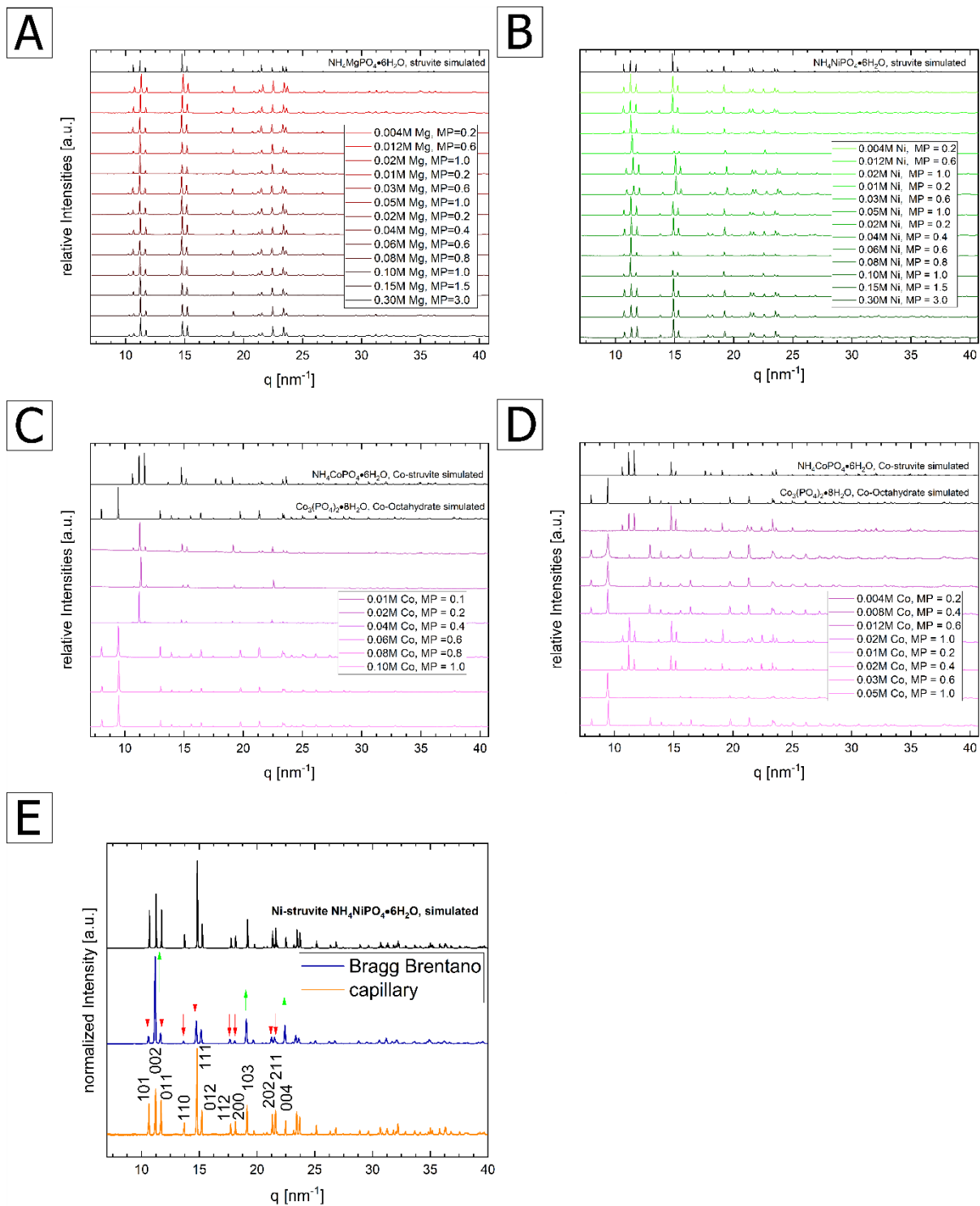


Figure 1A-E: stacked XRD patterns with the simulated pattern of the phosphate compound in black at first; These XRD patterns were used to create the phase stability diagrams; Mg-struvite reference COD 96-900-7675; Ni-struvite reference ICSD 403058; Co-struvite reference ICSD 170042; Co(II)phosphate octahydrate reference 2020362; In all measured XRD patterns of M-struvite preferred orientation of the (001) crystal planes occurred in a varying degree visible by strong intensity changes between simulated and measured pattern. All crystal planes with high (h00) or (0k0) component exhibit lower intensities while reflexes with a dominant (00l) component are intensified than in the simulated pattern visible in 1E. The preferred orientation is caused by the alignment of elongated habit of the crystals in the preparation of the flat powder sample holders

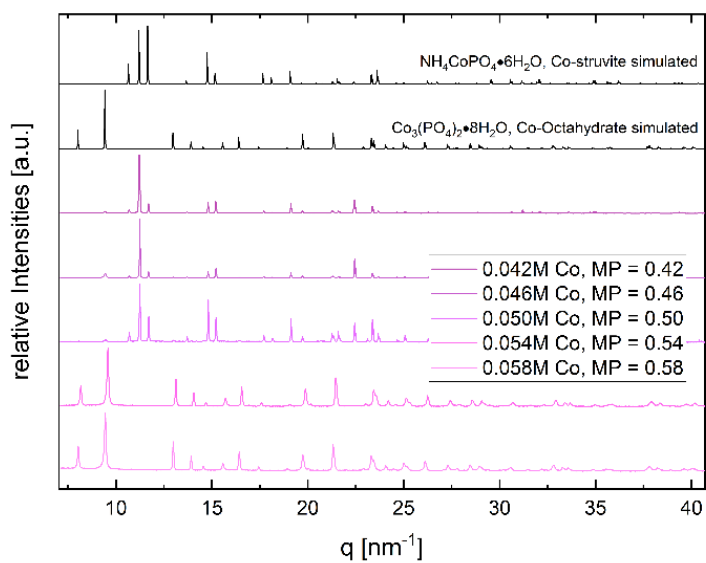
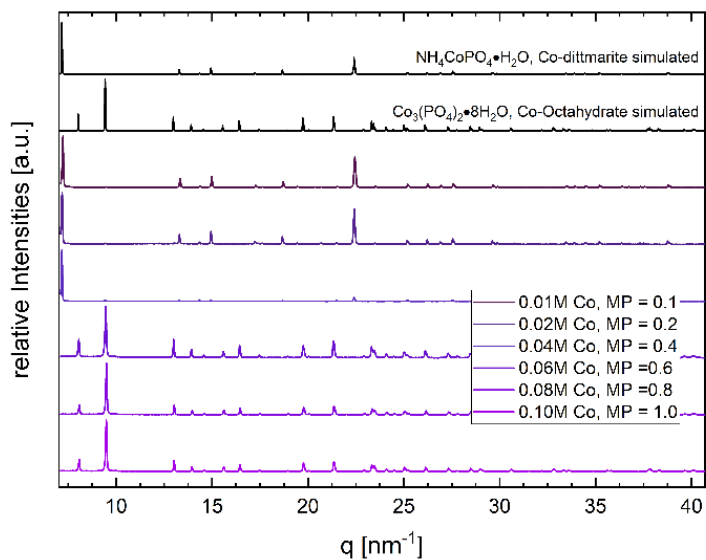
A**B**

Figure 2A and B: stacked XRD patterns with the simulated pattern of the phosphate compound in black at first; (A) In the transition interval between M/P ratios of 0.58-0.42 with 0.1 M DAP of the Co-system Co-struvite and Co(II) phosphate octahydrate are stable; (B) Co-struvite decomposes in air to Co-dittmarite while Co(II) phosphate octahydrate remains stable under these conditions. The same simulated patterns used as in Fig. 1 plus Co-dittmarite COD reference 2008122

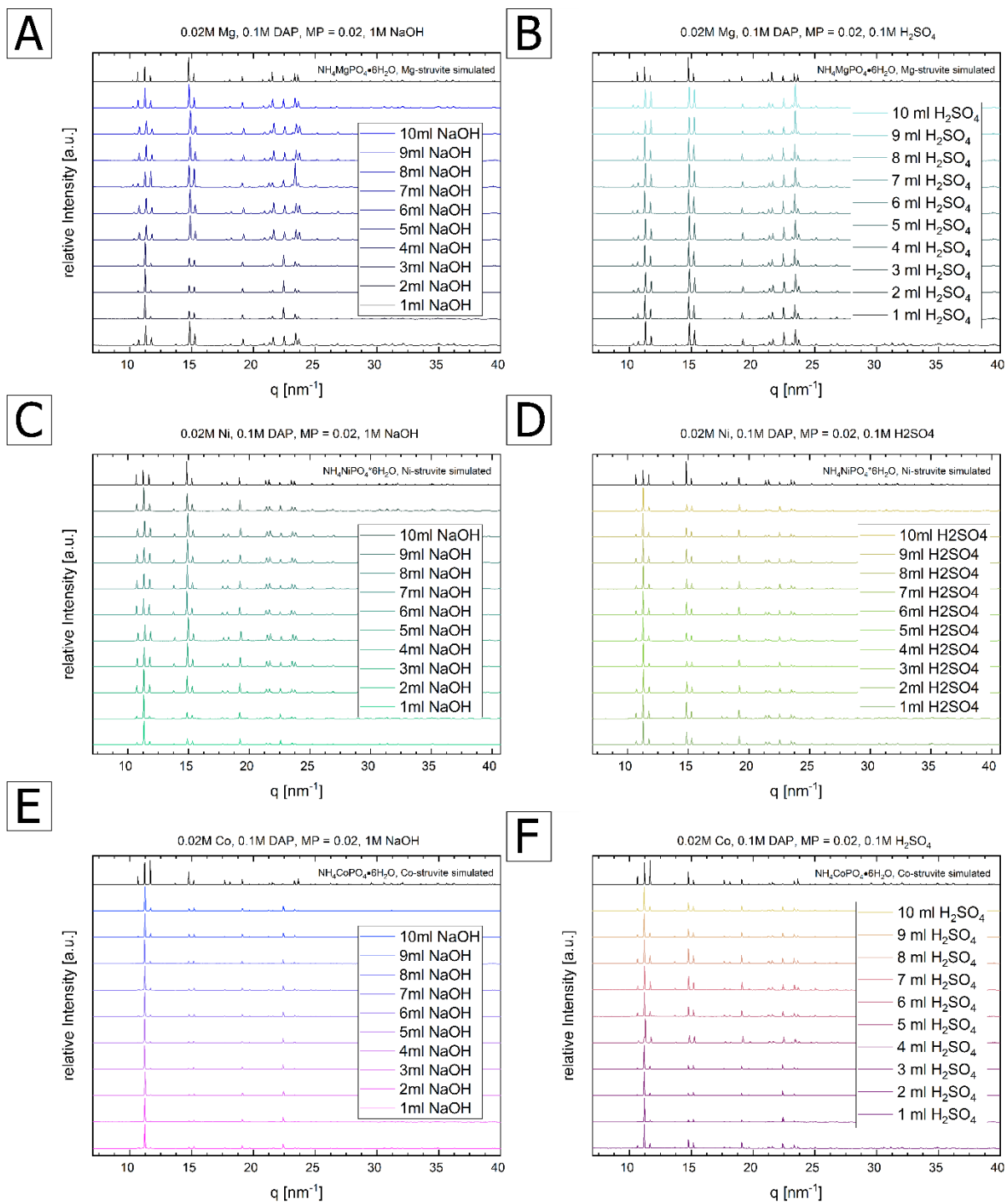


Figure 3A-F: pH adjusted samples with $\text{NaOH}_{(\text{aq})}$ and $\text{H}_2\text{SO}_{4(\text{aq})}$ of Mg (A, B), Ni (C, D) and Co (E, F) with their respective experimental conditions (caption) and their phase composition. In all samples single phase M-struvite precipitated; same simulated patterns used as in Fig. 1

Table 2: PHREEQC calculations of pH change in the solution with 100 ml 0.1M DAP and 100 ml of 0.02M M²⁺ (M = Mg, Co, Ni) plus different amounts of 1 M NaOH_(aq) (pH = 13.97) and 0.1 M H₂SO_{4(aq)} (pH = 1.00),

Experimental conditions		M/P ratio = 0.2		c(MSO ₄) [mM] = 20		c(DAP) [mM] = 100	
Sample with normal pH	amount of 1M NaOH _(aq) [ml]	calculated pH _{eq}	ΔpH	amount of 0.1M H ₂ SO _{4(aq)} [ml]	calculated pH _{eq}	ΔpH	
Ni-struvite pH _{eq} = 6.87	1	7.03	0.16	1	6.82	-0.05	
	2	7.21	0.33	2	6.78	-0.10	
	3	7.40	0.53	3	6.73	-0.15	
	4	7.66	0.78	4	6.68	-0.20	
	5	8.04	1.17	5	6.63	-0.25	
	6	8.47	1.60	6	6.57	-0.30	
	7	8.78	1.90	7	6.52	-0.35	
	8	8.99	2.12	8	6.46	-0.42	
	9	9.17	2.30	9	6.41	-0.47	
	10	9.32	2.45	10	6.35	-0.53	
Co-struvite pH _{eq} = 7.02	1	7.18	0.16	1	6.98	-0.04	
	2	7.37	0.35	2	6.94	-0.08	
	3	7.60	0.58	3	6.90	-0.12	
	4	7.89	0.87	4	6.86	-0.16	
	5	8.19	1.17	5	6.83	-0.19	
	6	8.38	1.36	6	6.79	-0.23	
	7	8.51	1.49	7	6.76	-0.26	
	8	8.59	1.57	8	6.72	-0.30	
	9	8.66	1.64	9	6.67	-0.35	
	10	8.75	1.73	10	6.61	-0.41	
Mg-struvite pH _{eq} = 7.33	5	8.86	1.84	5	6.99	-0.03	
	10	9.45	2.43	10	6.71	-0.62	

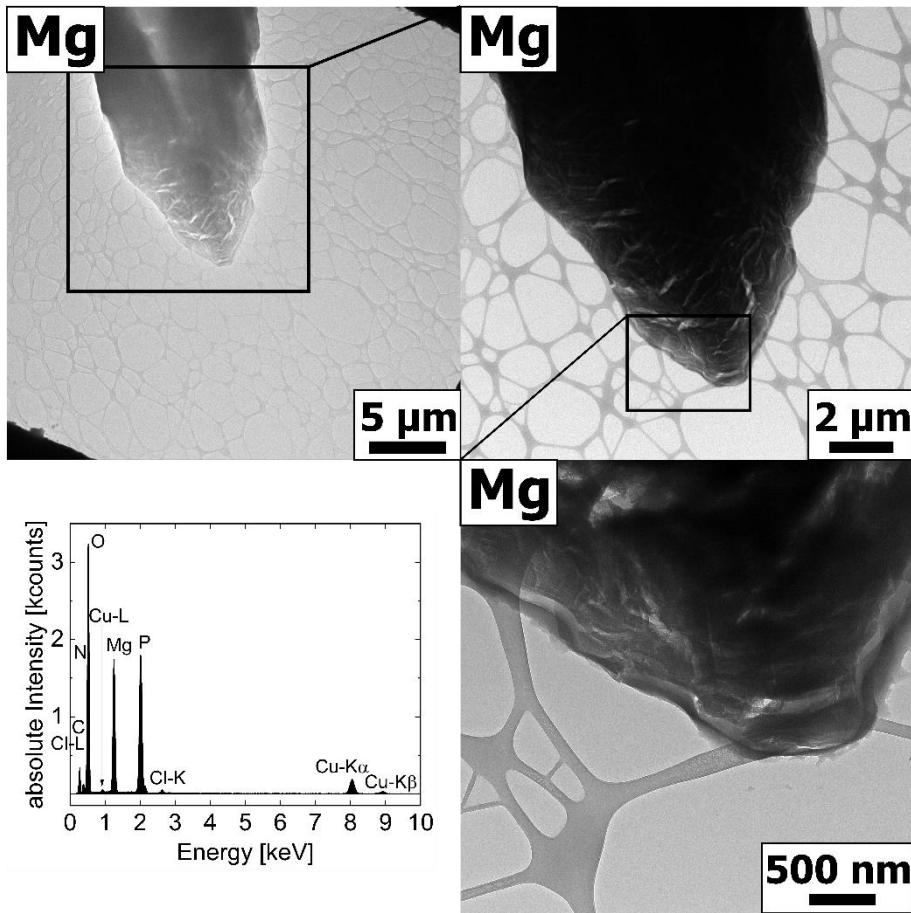


Figure 4 conventional TEM images of Mg sample after 5 seconds mixing forming crystals of μm size with visible vacuum cracks, lower left corner EDX spectrum of Mg-struvite

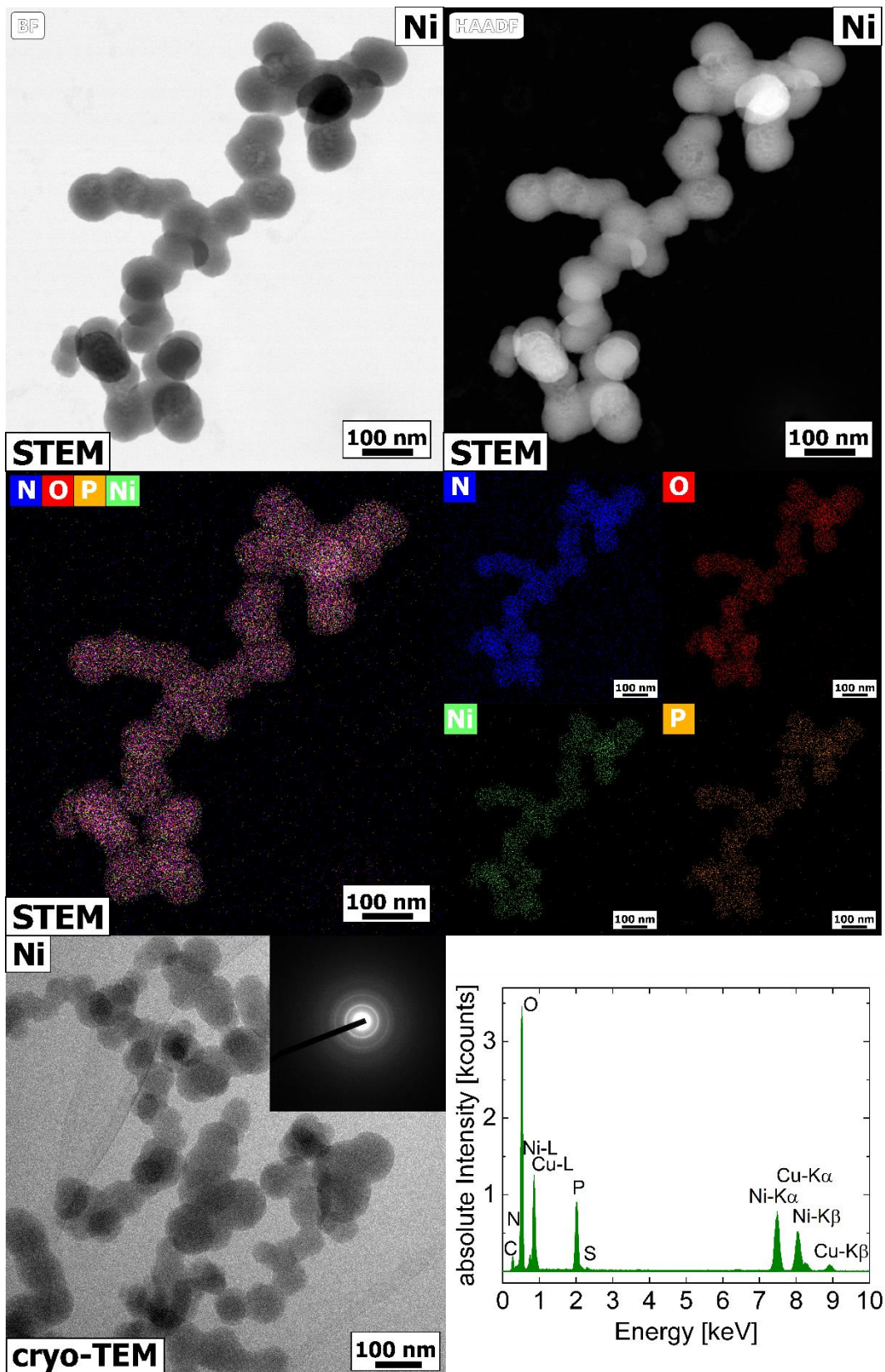


Figure 5: conventional STEM analysis of Ni sample after $t = 5$ sec mixing with the formation of amorphous nanoclusters in Bright field = BF, high angular dark field = HAADF and elemental mappings of N=Nitrogen, O=oxygen, Ni= nickel and P = phosphorus below with EDX point measurement; In the upper right corner cryo-TEM image of amorphous Ni-phase with SAED pattern

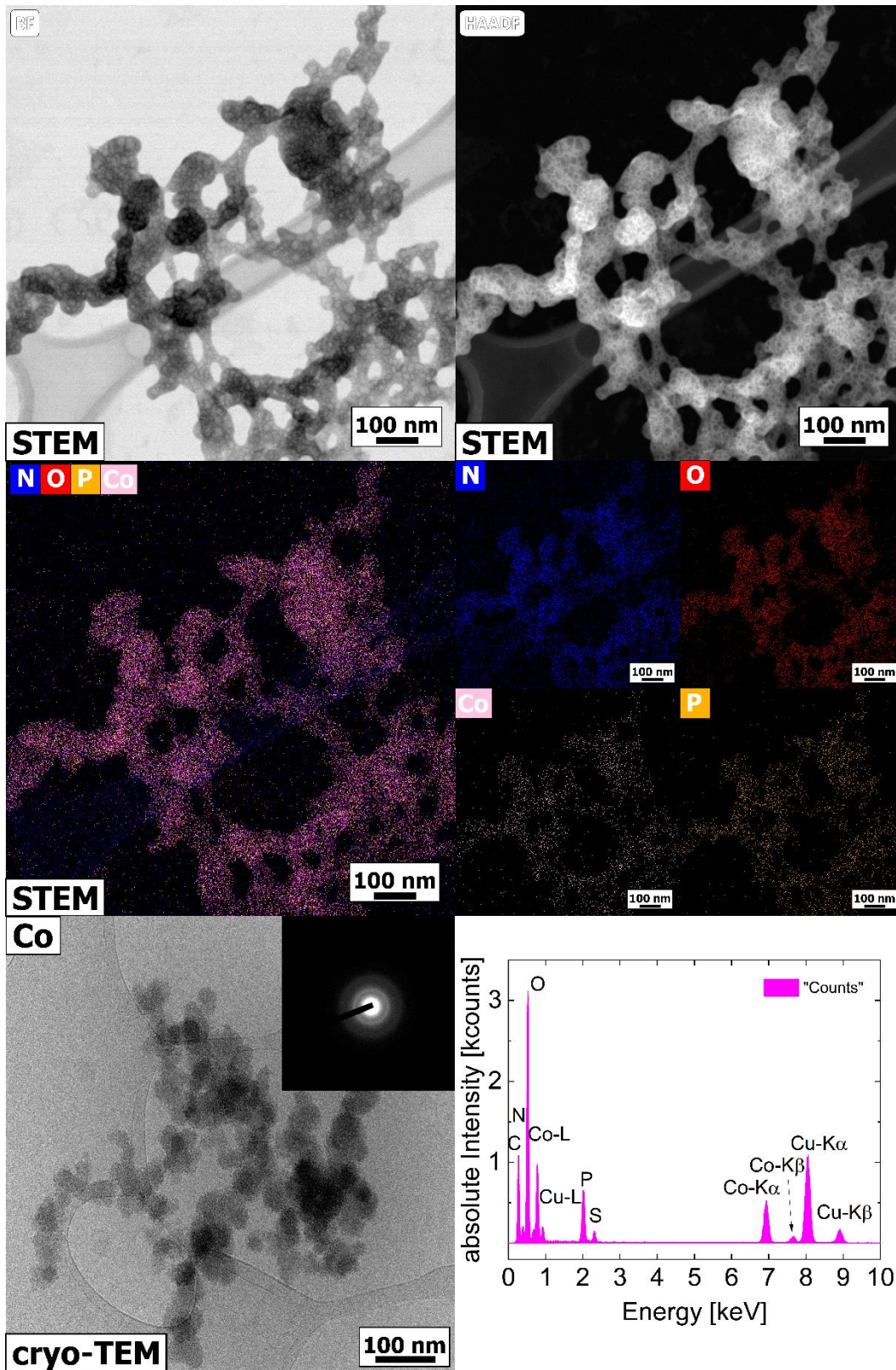


Figure 6: conventional STEM analysis of Co sample after $t = 5$ sec mixing with the formation of amorphous nanoclusters in Bright field = BF, high angular dark field = HAADF and elemental mappings of N=Nitrogen, O=oxygen, Co= cobalt and P = phosphorus below with EDX point measurement; In the upper right corner cryo-TEM image of amorphous Co-phase with SAED pattern

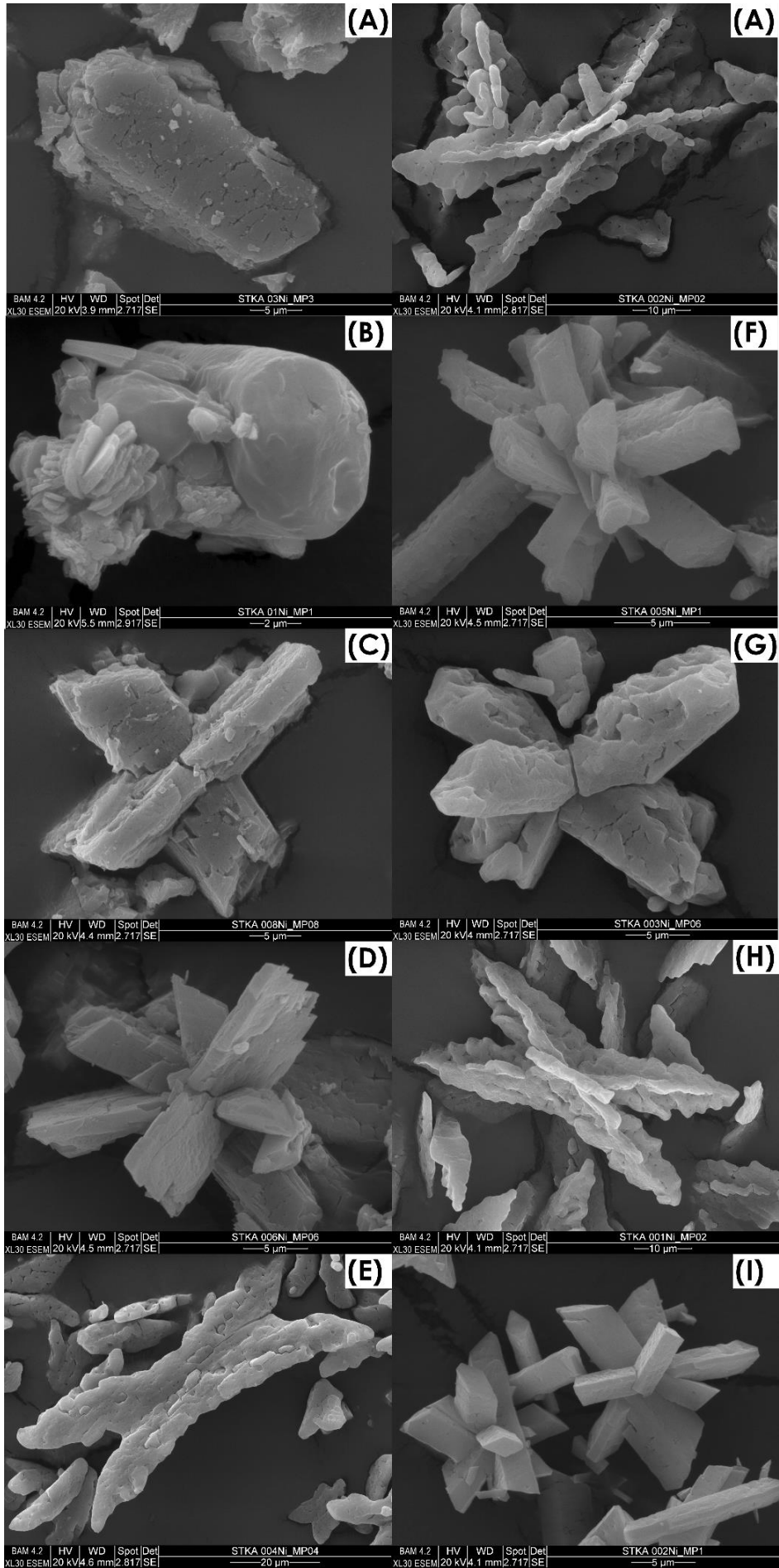


Figure 7A-J: Ni-struvite synthesized in varying concentrations of the educts (A: 0.3 M Ni, 0.1 M DAP, M/P ratio = 3; B: 0.1 M Ni, 0.1 M DAP, M/P ratio = 1; C: 0.08 M Ni, 0.1 M DAP, M/P ratio = 0.8; D: 0.06 M Ni, 0.1 M DAP, M/P ratio = 0.6; E: 0.04 M Ni, 0.1M DAP, M/P ratio = 0.4; F: 0.02 M Ni, 0.1 M DAP, M/P ratio = 0.2; G: 0.05 M Ni, 0.05 M DAP, M/P ratio = 1.0; H: 0.03 M Ni, 0.05 M DAP, M/P ratio = 0.6; I: 0.01 M Ni, 0.05M DAP, M/P ratio = 0.2; J: 0.02 M Ni, 0.02 M DAP, M/P ratio = 1.0)

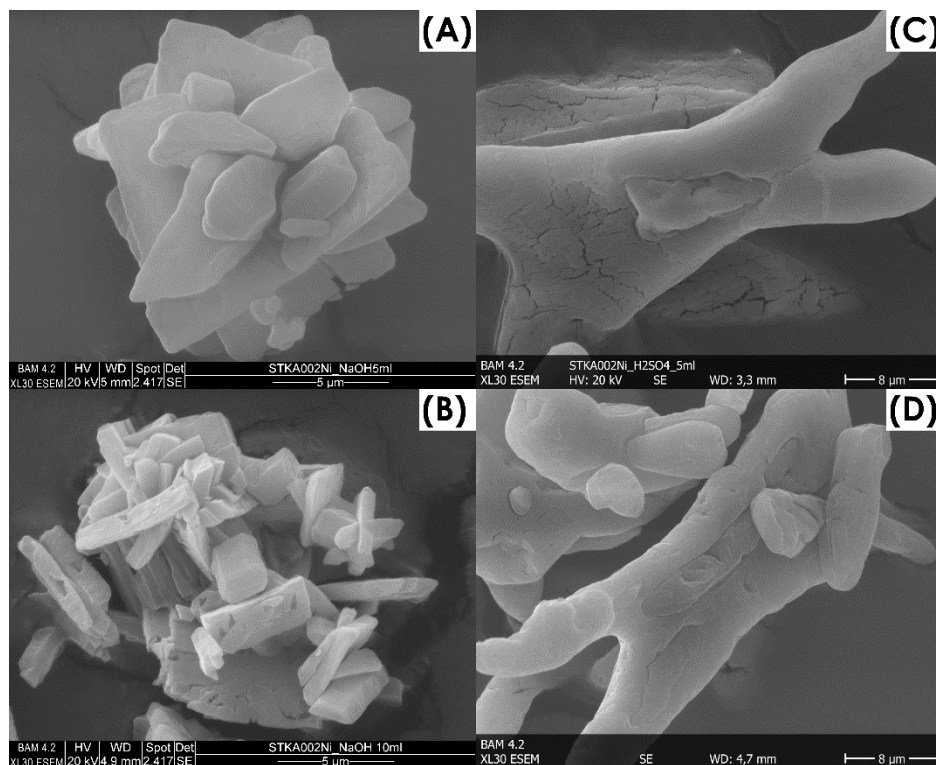


Figure 8A-D: Ni-struvite synthesized with 0.02 M Ni and 0.1 M DAP leading to a M/P ratio of 0.2 in different initial pH with 5 and 10 ml 1 M NaOH_(aq) or 0.1 M H₂SO_{4(aq)}; A: 5 ml 1M NaOH_(aq); B: 10 ml 1 M NaOH_(aq); C: 5 ml 1 M H₂SO_{4(aq)}; D: 10 ml 1 M H₂SO_{4(aq)};

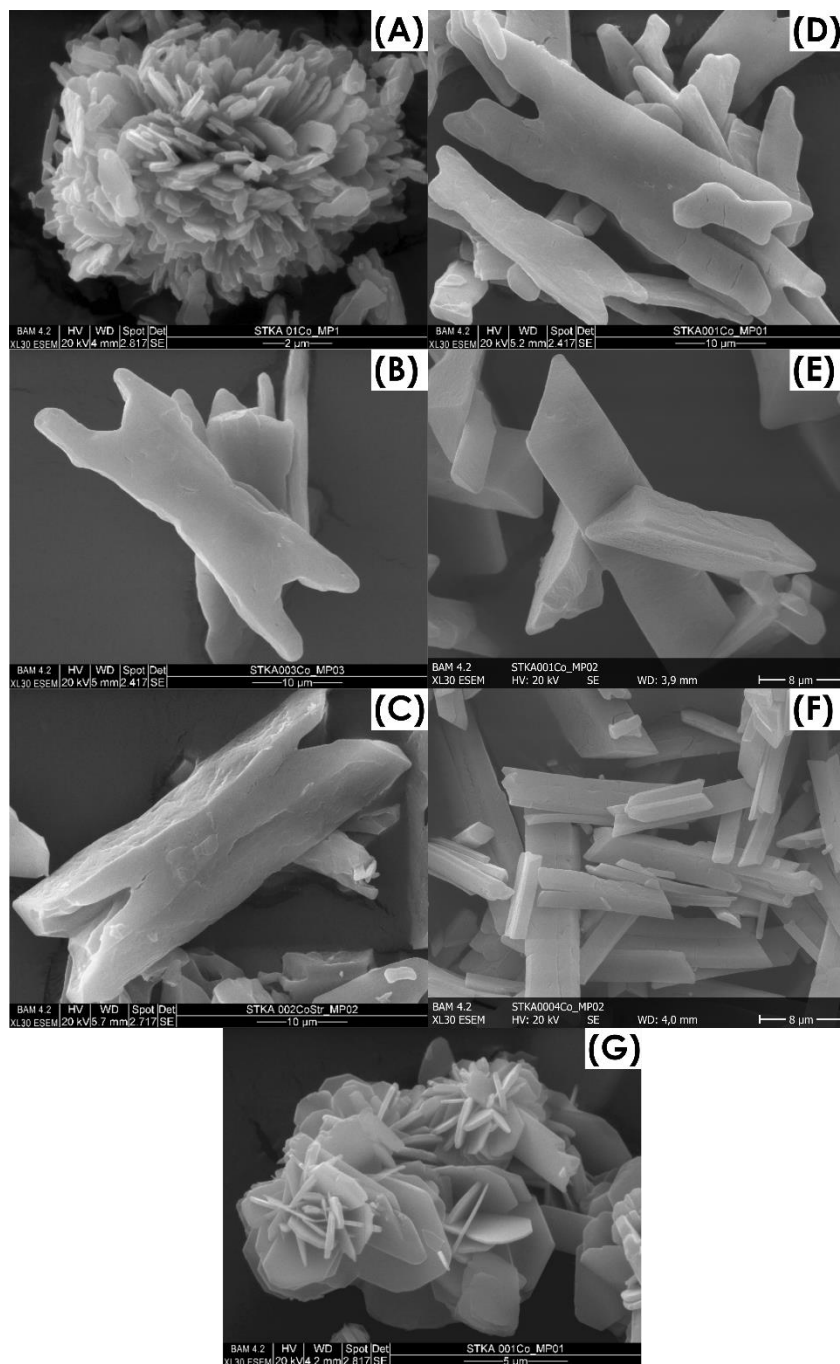


Figure 9A-G: Co-phosphates synthesized in different concentrations (A: Co(II)phosphate octahydrate 0.1 M Co, 0.1 M DAP, M/P ratio = 1; B: 0.03 M Co, 0.1 M DAP, M/P ratio = 0.3; C: 0.02 M Co, 0.1 M DAP, M/P ratio = 0.2; D: 0.01 M Co, 0.1 M DAP, M/P ratio = 0.1; E: 0.01 M Co, 0.05 M DAP, M/P ratio = 0.2; F: 0.004 M Co, 0.02 M DAP, M/P ratio = 0.2; G: Co-dittmarite in air decomposed 0.01 M Co, 0.1 M DAP, M/P ratio = 1.0)

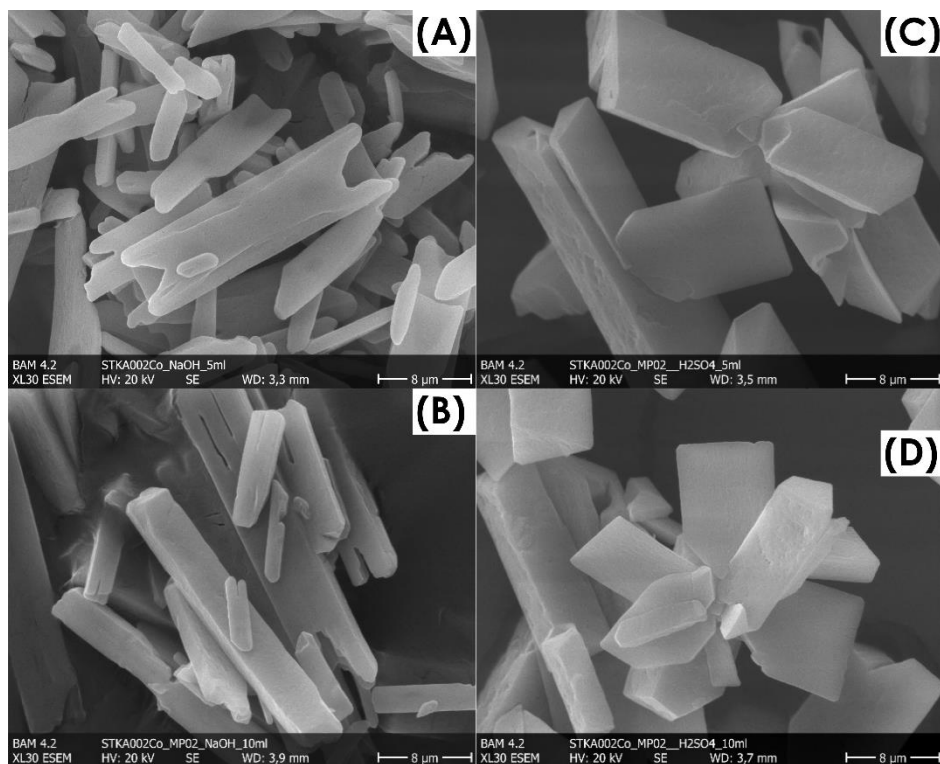


Figure 10A-D: Co-struvite synthesized with 0.02 M Ni and 0.1 M DAP leading to a M/P ratio of 0.2 in different initial pH with 5 and 10 ml 1 M NaOH_(aq) or 0.1M H₂SO_{4(aq)}; A:5 ml 1 M NaOH_(aq); B: 10 ml 1M NaOH_(aq); C: 5 ml 1 M H₂SO_{4(aq)}; D: 10 ml 1 M H₂SO_{4(aq)};

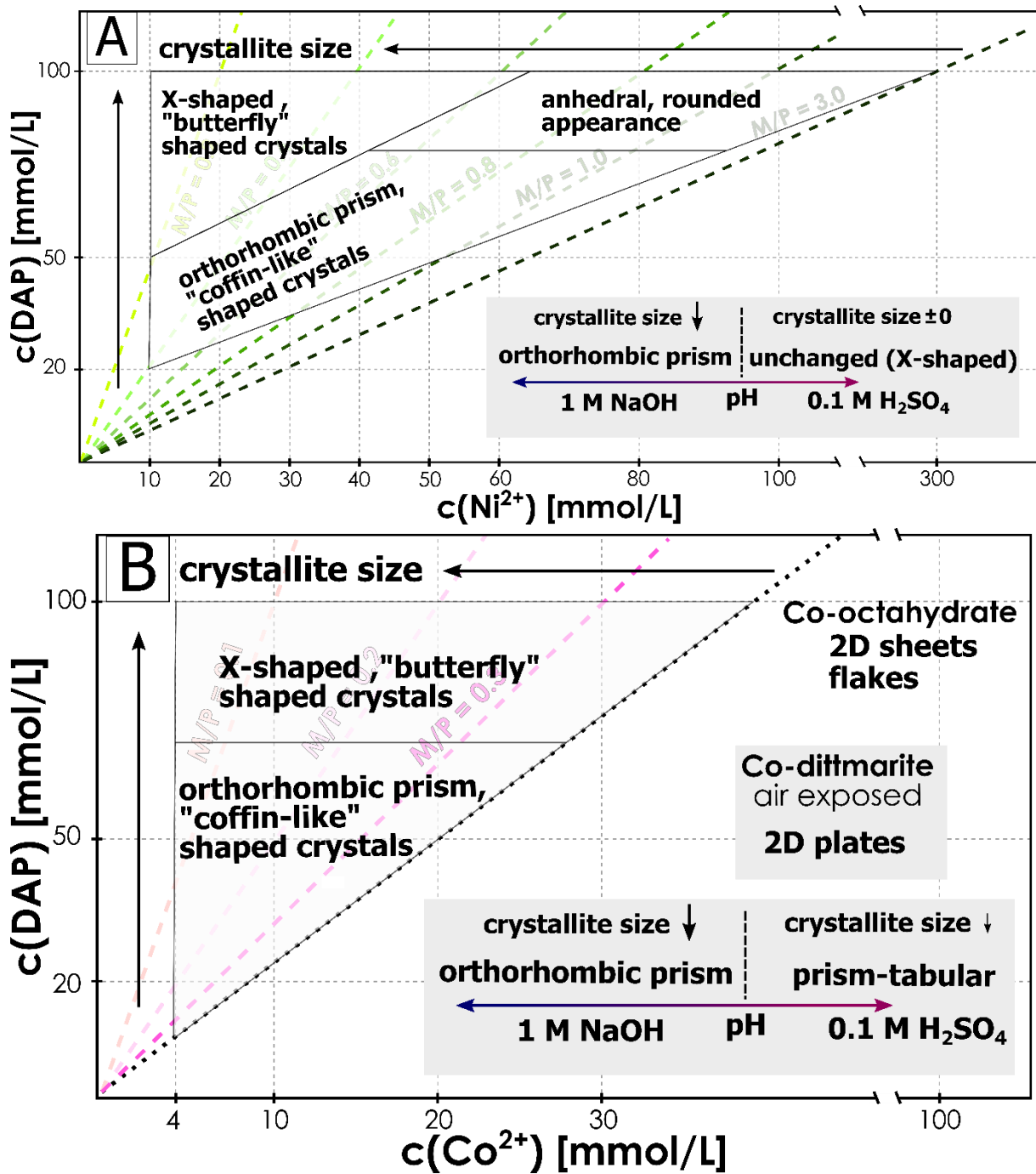


Figure 11A and B: Crystallization trends in the $c(M^{2+})$ vs. $c(DAP)$ plots with green (Ni, A)/ pink (Co, B) dotted lines indicating the distinct M/P ratio of the sample. Crystal Morphology fields are displayed in the triangles. The crystallite size increases with higher DAP and lower M^{2+} contents (see direction of the arrows); Adding $NaOH_{(aq)}$ decreased the crystallite size and favors the formation of orthorhombic prisms. Co-octahydrate exhibits a 2D sheet or flake morphology. By air exposure formed Co-dittmarite shows a 2D plate habit. In the Ni-system the crystallite size remained unchanged and while in the Co-system the crystals decreased slightly in size and habit to more tabular-shaped crystals.

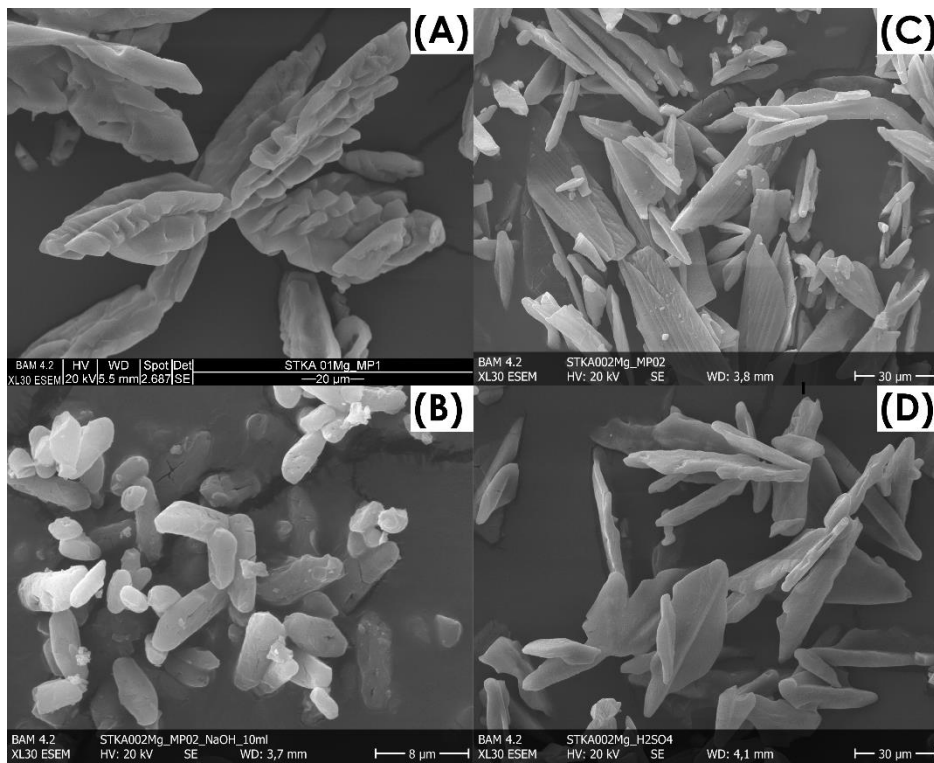


Figure 12A-D: Mg-struvite crystals synthesized at high (A: 0.1 M Mg, 0.1 M DAP, M/P ratio = 1) and low concentrations (B: 0.02M Mg, 0.1M DAP, M/P ratio = 0.2) plus pH adjusted low concentration samples with 10ml of C: sodium hydroxid NaOH_(aq) or D: sulfuric acid H₂SO_{4(aq)}

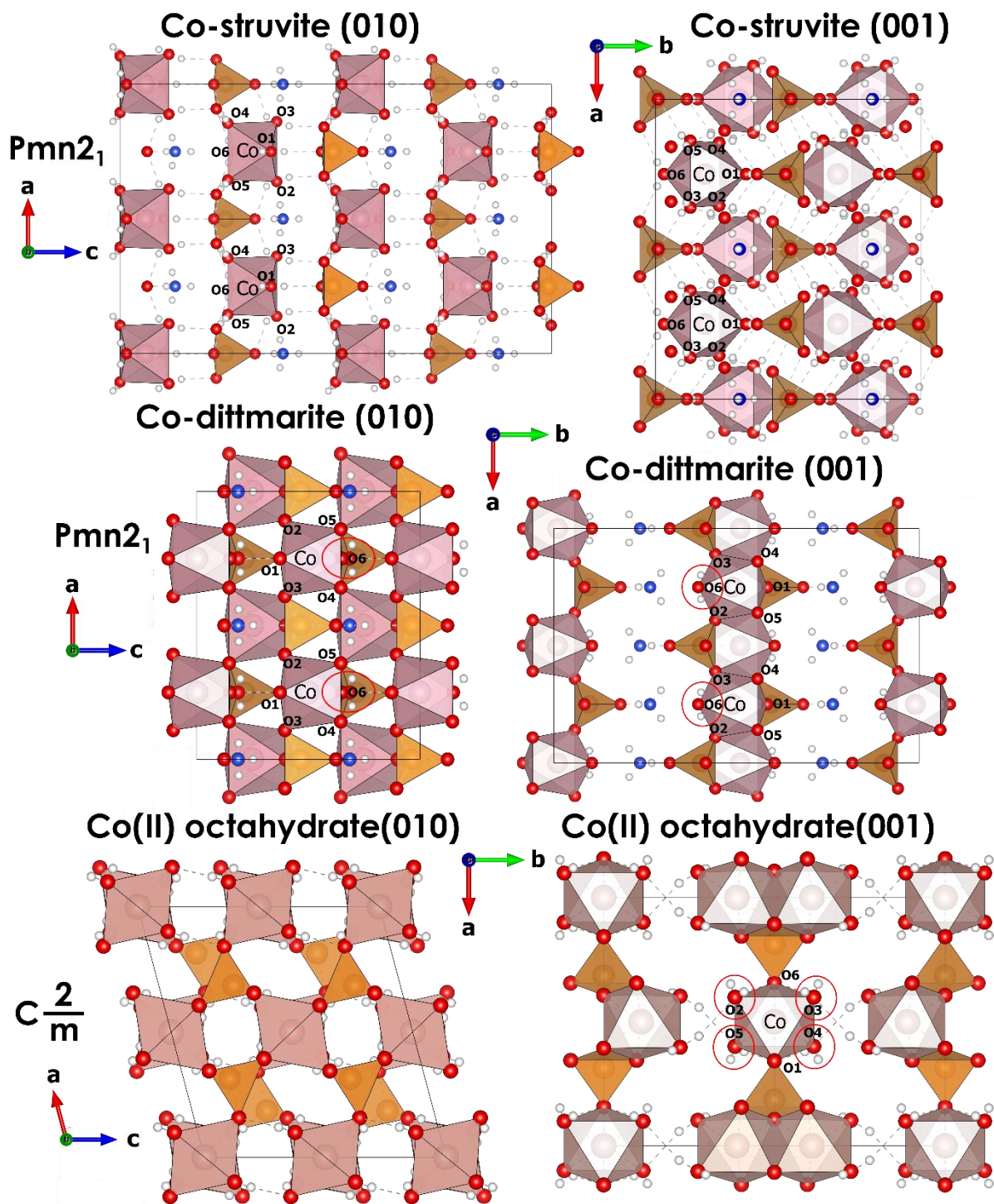


Figure 13: the (010) and (001) crystal planes of Co-struvite $\text{NH}_4\text{CoPO}_4 \cdot 6\text{H}_2\text{O}$, Co-dittmarite $\text{NH}_4\text{CoPO}_4 \cdot \text{H}_2\text{O}$ and Co(II)phosphate octahydrate $\text{Co}_3(\text{PO}_4)_2 \cdot 8\text{H}_2\text{O}$ crystal structure is displayed with the respective space group 31: $\text{Pmn}2_1$ for Co-struvite and Co-dittmarite (orthorhombic) and space group 12: C_2^2/m (monoclinic); Co: light pink, P: orange, Oxygen: red; Nitrogen; blue and hydrogen: white; one or two exemplary CoO_6 octahedrons are marked by atom labels with all the coordinating oxygen numbered; the coordinating crystal water in Co-dittmarite and Co-octahydrate is marked with red ellipsoids; note that in the Co-dittmarite and Co-octahydrate structure the CoO_6 is linked to the phosphate tetrahedrons while in the Co-struvite structure the CoO_6 is isolated by six coordinating crystal water oxygen

Table 3: Artemis fit parameter for Ni-struvite R-factor= 0.005, $\chi^2 = 3685.7$

sample	scattering path	degeneracy	σ^2	R_{diff} [Å]	R_{diff}^2 [Å ²]	R_{model} [Å]	R_{fit} [Å]
Ni-struvite	Ni1-O1	4	0.009	-0.001	1.00E-06	2.046	2.044
NH₄NiPO₄•6H₂O	Ni1-O2	2	0.009	-0.001	1.00E-06	2.089	2.088
mean R_{fit} (err) [Å]	Ni1-O3 H1	4	-0.001	-0.207	4.29E-02	2.560	2.353
2.059(6)	Ni1-H2	5	0.012	-0.217	4.70E-02	2.586	2.369
V_{sphere} (err) [Å ³]	Ni1-H3	2	0.012	-0.217	4.70E-02	2.627	2.410
36.6 (2)	Ni1-H4	2	0.012	-0.217	4.70E-02	2.668	2.451
χ^2	Ni1-O1-O1	6	-0.001	-0.207	4.29E-02	3.465	3.258
3685.7	Ni1-O3-O2	16	-0.001	-0.207	4.29E-02	3.530	3.322
R-factor	Ni1-N1	1	0.005	-0.186	3.47E-02	4.022	3.836
0.005	Ni1-N2	2	0.005	-0.186	3.47E-02	4.111	3.925
S_o^2 Amplitude reduction factor (err)	Ni1-O4	4	0.006	0.242	5.85E-02	4.084	4.326
	Ni1-O5	2	0.006	0.242	5.85E-02	4.162	4.404
1.3(1)	Ni1-O6	2	0.006	0.242	5.85E-02	4.200	4.442
ΔE (err)	Ni1-O7	3	0.006	0.242	5.85E-02	4.272	4.514
3.1(6)	Ni1-O8	2	0.006	0.242	5.85E-02	4.329	4.571

Table 4: Artemis fit parameter for Co-struvite R-factor= 0.012, $\chi^2 = 8650.5$

sample	scattering path	degeneracy	σ^2	$R_{\text{diff}} [\text{\AA}]$	$R_{\text{diff}}^2 [\text{\AA}^2]$	$R_{\text{model}} [\text{\AA}]$	$R_{\text{fit}} [\text{\AA}]$
Co-struvite	Co1-O1	2	0.005	0.0001	1.69E-08	2.058	2.058
NH₄CoPO₄•6H₂O	Co1-O2	2	0.005	0.0001	1.69E-08	2.089	2.089
mean R_{fit} (err) [\AA]	Co1-O3	2	0.005	0.0001	1.69E-08	2.129	2.129
2.091(1)	Co1-H1	2	0.003	0.3078	9.48E-02	2.211	2.519
V_{sphere} (err) [\AA^3]	Co1-H2	2	0.003	0.3078	9.48E-02	2.451	2.759
38.35(2)	Co1-H3	4	0.003	0.3078	9.48E-02	2.549	2.857
χ^2	Co1-H4	2	0.003	0.3078	9.48E-02	2.616	2.924
8650.5	Co1-O1-H3-O1	4	0.003	0.3774	1.42E-01	2.752	3.129
R-factor	Co1-O5-O6-O5	2	0.003	0.3774	1.42E-01	2.840	3.217
0.012	Co1-O3-H5-O3	1	0.003	0.3774	1.42E-01	2.843	3.220
S_o^2 Amplitude reduction factor (err)	Co1-O1-O2	6	-0.003	0.2301	5.29E-02	3.507	3.737
	Co1-O1-O3	12	-0.003	0.2301	5.29E-02	3.575	3.805
0.85(5)	Co1-O2-O3	4	-0.003	0.2301	5.29E-02	3.622	3.852
ΔE (err)	Co1-N1	1	0.001	-0.0171	2.94E-04	4.027	4.009
4.5(6)	Co1-N2	2	0.001	-0.0171	2.94E-04	4.133	4.115
	Co1-O4	4	0.003	0.3774	1.42E-01	4.105	4.482
	Co1-O6	4	0.003	0.3774	1.42E-01	4.199	4.576
	Co1-O7	3	0.003	0.3774	1.42E-01	4.288	4.665
	Co1-O8	2	0.003	0.3774	1.42E-01	4.362	4.739
	Co1-P1	2	0.003	0.3774	1.42E-01	4.393	4.770

Table 5: Artemis fit parameter for Co-dittmarite (COD), R-factor= 0.008, $\chi^2 = 4430.7$

sample	scattering path	degeneracy	σ^2	R_{diff} [Å]	R_{diff} [Å ²]	R_{model} [Å]	R_{fit} [Å]
Co-dittmarite	Co1-O1	3	0.001	0.0001	1.69E-08	2.055	2.023
NH ₄ CoPO ₄ •H ₂ O	Co1-O2	3	0.001	0.0001	1.69E-08	2.201	2.169
mean R_{fit} (err) [Å]	Co1-H1	2	-0.008	0.0001	1.69E-08	2.492	2.222
2.096(1)	Co1-H2	2	-0.008	0.3078	9.48E-02	2.970	2.699
V_{sphere} (err)[Å ³]	Co1-P1	1	0.002	0.3078	9.48E-02	2.797	2.797
38.55(2)	Co1-P2	2	0.002	0.3078	9.48E-02	3.209	3.209
χ^2	Co1-O3	2	0.001	0.2301	5.29E-02	3.313	3.281
4430.7	Co1-P3	1	0.002	0.3078	9.48E-02	3.305	3.305
R-factor	Co1-O4	2	0.001	-0.0171	2.94E-04	3.592	3.560
0.008	Co1-Co2	7	0.010	0.3774	1.42E-01	3.712	3.653
S_o^2 Amplitude reduction factor	Co1-O5	1	0.001	-0.0171	2.94E-04	3.753	3.721
0.796(57)	Co1-N1	1	-0.008	0.3774	1.42E-01	4.010	3.740
ΔE	Co1-O6	3	0.001	0.2301	5.29E-02	3.813	3.781
2.657(619)	Co1-O7	1	0.001	0.2301	5.29E-02	3.944	3.912

Table 6: Artemis fit parameter for Co-phosphate octahydrate (CPO), R-factor= 0.005, $\chi^2 = 2393.42$

sample	scattering path	degeneracy	σ^2	$R_{diff} [\text{\AA}]$	$R_{diff}^2 [\text{\AA}^2]$	$R_{model} [\text{\AA}]$	$R_{fit} [\text{\AA}]$
Co-octahydrate	Co1-O1	5	0.011	-0.003	8.53E-06	2.021	2.099
Co₃(PO₄)₂•8H₂O	Co1-O2	1	0.011	-0.003	8.53E-06	2.158	2.155
mean R_{fit} (err) [\AA]	Co1-H1	16	0.018	-0.079	6.19E-03	2.451	2.372
2.11(2)	Co1-O2-H2	8	0.001	0.416	1.73E-01	2.593	2.593
V_{sphere} (err)[\AA^3]	Co1-H3	4	0.018	-0.079	6.19E-03	3.226	3.147
39.3(6)	Co1-P1	2	0.010	-0.003	9.18E-06	3.194	3.191
χ^2	Co1-H3	8	0.018	-0.079	6.19E-03	3.319	3.240
2393.42	Co1-O3	4	0.001	0.416	1.73E-01	3.579	3.389
R-factor	Co1-O1-O2	8	-0.013	0.099	9.82E-03	3.553	3.553
0.005	Co1-O5	2	0.010	-0.003	9.18E-06	3.675	3.576
S_o^2 Amplitude reduction factor (err)	Co1-O1-O2	8	-0.013	0.099	9.82E-03	3.584	3.584
	Co1-O2-O2	8	0.010	-0.003	9.18E-06	3.684	3.672
1.319	Co1-O1-P1	4	-0.013	0.099	9.82E-03	3.389	3.684
ΔE	Co1-O4	8	0.010	-0.003	9.18E-06	3.950	3.947
4.909	Co1-H3-O4	16	0.001	0.416	1.73E-01	4.014	4.014
	Co1-O6-H5	8	0.001	0.416	1.73E-01	4.450	4.450

Outlook

Cobalt is also classified as a CRM according to the EU, because it is used in a number of technological applications [accumulators for example as cathode material in lithium-ion batteries, superalloys, catalysators], but it is only exploitable in few ore deposits in the world, most lying in the Democratic Republic of Congo. There it is concentrated in minerals such as the Cobaltite [CoAsS], erythrite [Co₃(AsO₄)₂·8H₂O] or skutterudite [CoAs₃] in hydrothermal altered mantle rocks in association with mainly nickel. Although, it plays an essential role in several enzymes and co-enzymes involved in the metabolism of animals and plants for example vitamin B12 alias cobalamin. In above trace concentrations cobalt is highly toxic. The aforementioned nickel is widely used in the industry and is also relatively common. It is mined in lateritic ultramafic rocks from ore minerals like pentlandite [(Ni,Fe)₈S₉] or nickelferrous limonite [(Ni,Fe)O(OH)]. Unfortunately, in the environment nickel compounds cause numerous carcinogenic effects in human and plants and it is one of the most rated allergen in the world. This is even though at trace concentrations it plays also an important biological role for plants and microbes as a part of enzymes such as urease [1, 2]. Hence although nickel is not a CRM, it should be recovered from wastewater.

In mining waters of the Eshidiya mine (Jordan) the PO₄³⁻ and NH₄⁺ content in mining waste waters ranges from 8.9-0.1 mg/l and 0.95-0.03 mg/l, respectively (Al-Hwaiti et al. 2016). The related ground water in the same region showed concentrations values of PO₄³⁻ and NH₄⁺ 3.8-3.5 and 0.05-0.01 mg/l. Mine waste waters from the Duluth Gabbro complex in Minnesota (USA) contain average values of 198 mg/l of Ni and 9.8 mg/l of Co (Hammack et al. 1991). In the Katanga province (DRC) in effluent surface mine waters of a Co-Cu ore deposit Co reached maximum concentrations of 3164 µg/l (Atibu et al. 2013). In Rio Piscianas (Italy) the highly contaminated groundwater from mining activities in the 90s had concentrations of 2900-1500 µg/l for Co and 4600-3000 µg/l for Ni (Concas et al 2006). Ground water samples from the Amik plain (Turkey) contain in average 13 mg/l NH₄⁺, 87 mg/l Phosphorus, 13 µg/l Co and 50 µg/l Ni (Agca et al. 2014).

These numbers prove that transition metals as well as ammonia and phosphate are common contaminants in ground and waste waters. As mining wastewaters contain high amounts of transition metals (mg/l) at low pH (~4-5) while agricultural waste- and groundwaters demonstrate high concentrations of phosphate and ammonium at medium to high pH (7-9) a mixture of both waste waters could lead to precipitation of M-struvite in significant amounts. By mixing different waste waters together multiple environmental critical compounds could be extracted simultaneously. Further experiments to the up scalability and implementation as wastewater treatment method would quantitatively evaluate if the precipitation of M-struvite is applicable as wastewater treatment method or not.

Table 7: concentrations of Co, Ni, ammonia NH_4^+ and phosphate PO_4^{3-} /total phosphorus (TP) in different waste waters in mg/L otherwise unit displayed; agricultural waste waters contain high amounts of ammonia and phosphorus while mine waste waters demonstrate high conc. of heavy metals

country	region	waste water	species	concentration	reference
DRC	Katanga province	mine waste water	Co	3.164	Atibu et al.2013 [3]
Italy	Rio Piscinas	ground water (contaminated)	Co	2.9-1.5	Concas et al. 2006 [4]
			Ni	4.6-3.0	
Turkey	Amik plain	agricultural waste water	NH_4^+	13	Agca et al. 2014 [5]
			TP	87	
			Co	13 [$\mu\text{g/L}$]	
			Ni	50 [$\mu\text{g/L}$]	
USA	Duluth gabbro, Minnesota	mine waste water	Co	9.8	Hammack et al. 1991 [6]
			Ni	198	
Jordan	Eshidiya mine	mine waste water	NH_4^+	95-30[$\mu\text{g/L}$]	Al-Hwaiti et al. 2016 [7]
			PO_4^{3-}	8.9-0.1	
		ground water	NH_4^+	3.8-3.5	Al-Hwaiti et al. 2016 [7]
			PO_4^{3-}	50-10 [$\mu\text{g/L}$]	
Zambia	Kabwe	mine waste water	Co	34,400	Sracek et al .2010 [8]
China	Sichuan	agricultural waste water	NH_4^+	1257.14	Feng et al. 2020 [9]
			PO_4^{3-}	25.01	
Brazil		agricultural waste water	NH_4^+	77	Leite et al. 2009 [10]
			TP	12	
USA	Cobalt, Ontario	surface water	Co	2028-0.5 [$\mu\text{g/L}$]	Percival et al. 1996 [11]
			Ni	660-2.6 [$\mu\text{g/L}$]	
Serbia	Bor	mine waste water	Ni	6128	Stopic et al. 2007 [12]
			Co	1.2	

References SI

- [1] Carter EL, Flugga N, Boer JL, Mulrooney SB, Hausinger RP. Interplay of metal ions and urease. *Metallomics*. 2009;1(3):207-21.
- [2] Mazzei L, Musiani F, Ciurli S. The structure-based reaction mechanism of urease, a nickel dependent enzyme: tale of a long debate. *J Biol Inorg Chem*. 2020;25(6):829-45.
- [3] Atibu EK, Devarajan N, Thevenon F, Mwanamoki PM, Tshibanda JB, Mpiana PT, et al. Concentration of metals in surface water and sediment of Luilu and Musonoie Rivers, Kolwezi-Katanga, Democratic Republic of Congo. *Applied Geochemistry*. 2013;39:26-32.
- [4] Concas A, Ardau C, Cristini A, Zuddas P, Cao G. Mobility of heavy metals from tailings to stream waters in a mining activity contaminated site. *Chemosphere*. 2006;63(2):244-53.
- [5] Agca N, Karanlik S, Odemis B. Assessment of ammonium, nitrate, phosphate, and heavy metal pollution in groundwater from Amik Plain, southern Turkey. *Environ Monit Assess*. 2014;186(9):5921-34.
- [6] Hammack R, Edenborn H. the removal of nickel from mine waters using bacterial sulfate reduction. *Proceedings America Society of mining and Reclamation*. 1991:97-108.
- [7] Al-Hwaiti MS, Brumsack HJ, Schnetger B. Suitability assessment of phosphate mine waste water for agricultural irrigation: an example from Eshidiya Mines, South Jordan. *Environmental Earth Sciences*. 2016;75(3).
- [8] Sracek O, Mihaljevič M, Kříbek B, Majer V, Veselovský F. Geochemistry and mineralogy of Cu and Co in mine tailings at the Copperbelt, Zambia. *Journal of African Earth Sciences*. 2010;57(1-2):14-30.
- [9] Feng C, Zhang S, Wang Y, Wang G, Pan X, Zhong Q, et al. Synchronous removal of ammonium and phosphate from swine wastewater by two agricultural waste based adsorbents: Performance and mechanisms. *Bioresour Technol*. 2020;307:123231.
- [10] Leite V, Athayde Junior G, Sousa J, Lopes W, Henrique I. Treatment of Domestic Wastewater in Shallow Waste Stabilization Ponds for Agricultural Irrigation Reuse. *Journal of Urban and Environmental Engineering*. 2009;3(2):58-62.
- [11] Percival J, Dumaresq C, Kwong Y, Hendry K, Michel F. Arsenic in surface waters, Cobalt, Ontario. *Current Reserach* 1996-C. 1996:137-46.
- [12] Stopic S, Pavlovic J, Friedrich B. treatment of Highly Contaminated Waste Waters in a Continous Cascade Line Reactor. *World of metallurgy - ERZMETALL*. 2007;60:255-62.